Ionospheric Disturbances and Irregularities During the 25-26 August 2018 Geomagnetic Storm

E. Astafyeva, Y. Yasyukevich, B. Maletckii, A. Oinats, A. Vesnin, A. Yasyukevich, S. Syrovatskii, N. Guendouz

Ionospheric disturbances and irregularities during the 25-26 August 2018 geomagnetic storm

E. Astafyeva[1], Yu. V. Yasyukevich[2], B. Maletckii[1,2], A. Oinats[2], A. Vesnin[2], A.S. Yasyukevich[2], S. Syrovatskii[3], N. Guendouz[1]

1 – Université de Paris, Institut de Physique du Globe de Paris (IPGP), CNRS UMR 7154, 35-39
Rue Hélène Brion, 75013 Paris, email : astafyeva@ipgp.fr
2 – Institute of Solar-Terrestrial Physics, Siberian Branch of Russian Academy of Sciences,
126a Lermontova street, Irkutsk, Russian Federation, email: yasyukevich@iszf.irk.ru
3 – Moscow State University, Moscow, email: semen_syrovatskii@iszf.irk.ru

Abstract

We use ground-based (GNSS, SuperDARN, ionosondes) and space-borne (Swarm, CSES, DMSP) instruments to study ionospheric disturbances due to the 25-26 August 2018 geomagnetic storm. The strongest large-scale storm-time enhancements were detected over the Asian and Pacific regions during the main and early recovery phases of the storm. In the American sector, there occurred the most complex effects caused by the action of multiple drivers. At the beginning of the storm, a large positive disturbance occurred over North America at low and high latitudes, driven by the storm-time reinforcement of the equatorial ionization anomaly (at low latitudes) and by particle precipitation (at high latitudes). During local night-time hours, we observed numerous medium-scale positive and negative ionospheric disturbances at middle and high latitudes that were attributed to a storm-enhanced density (SED)-plume, mid-latitude ionospheric trough and particle precipitation in the auroral zone. In South America, total electron content (TEC) maps clearly showed the presence of the equatorial plasma bubbles, that, however, were not seen in data of Rate-of-TEC-change index (ROTI). Global ROTI maps revealed intensive small-scale irregularities at high-latitudes in both hemispheres within the auroral region. In general, the ROTI disturbance "imaged" quite well the auroral oval boundaries. The most intensive ionospheric fluctuations were observed at low and mid-latitudes over the Pacific Ocean. The storm also affected the positioning accuracy by GPS receivers: during the main phase of the storm, the precise point positioning error exceeded 0.5 m, which is more than 5 times greater as compared to quiet days.

Key words: geomagnetic storms, ionosphere, ionospheric disturbances, multi-instrumental approach, ionospheric irregularities, ROTI

1. Introduction

Ionospheric disturbances due to geomagnetic storms, that are often referred to as "Ionospheric storms", are extremely manifold and diverse in their manifestations. The storm affects the ionosphere globally, and produces disturbances of different spatial and temporal scales.

The storm-time ionosphere behaviour is controlled by several competing dynamic and electro-dynamic processes, known as drivers. Penetration of electric fields of magnetospheric origin (i.e., prompt penetration electric fields, PPEF), the disturbance dynamo electric fields, and the interaction between ions and neutrals are the main drivers causing increases (positive storms) or decreases (negative storm) in the ionospheric plasma parameters with respect to the quiet-time values (e.g., Fuller-Rowell, 2011).

Recent development of networks of ground-based instruments and the launch of new satellite missions allowed to reveal new aspects of the ionospheric and thermospheric behaviour during magnetic storms with unprecedented details (e.g., Tsurutani et al., 2004; 2016; Yizengaw et al., 2005, 2006; Foster and Rideout, 2005; Huang et al., 2005; Foster & Coster, 2007; Astafyeva et al., 2007; 2015b; 2016a,b; 2017; 2018; Valladares et al., 2017; Lei et al., 2014; Zou et al., 2014; Cherniak et al., 2018; Zakharenkova et al., 2016b; 2019; Zakharenkova and Cherniak, 2020; Ngwira et al., 2019). However, despite numerous efforts, the ionospheric storms remain the biggest challenge for correct modelling and space weather forecasts.

The 25-26 August 2018 storm arrived as a surprise to forecasters. It was initiated by a weak CME that was not detected automatically, and was recognized as "minorly geoeffective" only after additional manual analysis [Vanlommel et al., 2018]. The CME's arrival did not cause a sudden impulse and was not captured by ground-based magnetometers. However, while it arrived nearly unnoticed, the CME triggered major disturbances in the magnetosphere, ionosphere and thermosphere [e.g., Blagoveschensky and Sergeeva, 2019 Astafyeva et al., 2020; Piersanti et al., 2020; Younas et al., 2020; Bolaji et al., 2021; Spogli et al. 2021]. Blagoveschensky and Sergeeva (2019) studied ionospheric response over Europe and observed positive disturbance at mid and low latitudes during the main phase. They also reported blackouts that occurred due to the high absorption level at high latitudes. Astafyeva

et al. (2020) studied thermospheric and ionospheric response to the August 2018 storm in the American and Pacific sectors and noticed the unprecedented hemispheric asymmetry in the ionosphere storm-time redistribution, and especially in the thermospheric composition. Strong positive storm was observed during the main phase of the storm over North America. While, in southern hemisphere, no effects occurred during this period of time. The second day of the storm showed quite significant negative storm effects in the VTEC and the Ne in the American sector, especially over North America. Spogli et al. (2021) completed the latter study by focusing on electromagnetic and ionospheric variations over South America. They showed significant longitudinal difference in the electrodynamic behaviour between the Western and Eastern South American sectors. Such effects led to different ionospheric patterns on the west (increase) and east (decrease) coasts of South America.

In this work, for the first time, we provide a detailed global multi-instrumental overview of the ionospheric effects caused by the August 2018 storm, and we analyse the occurrence of the irregularities in TEC and electron density during this storm. In addition, we suggest a new method of processing of the electron density data of the recent CSES mission [Shen et al., 2018].

2. Data & Methodology

In this work, we analyze the following set of parameters:

1) **Absolute vertical total electron content (VTEC)** as derived from data of ground-based GNSS receivers. The VTEC is calculated from phase and code measurements and by removing the satellite and receiver biases [Rideout and Coster, 2006; Zakharenkova et al., 2016; Yasukevich et al., 2020b]. In this work, we use VTEC data with 5-min resolution that are available from the OpenMadrigal database [Rideout and Coster, 2006]. To assess the storm-time VTEC alterations (dVTEC), we remove 7-day averaged quiet-time reference values from the storm-time values. The latter was calculated by using data of 7 least perturbed days in August-September 2018. The TEC is measured in TEC units (TECU), with 1 TECU equal to 10^{16} electrons/m^2.

104

2) **Rate-of-TEC change Index (ROTI)** was calculated from the slant TEC. The ROTI is an index characterizing the intensity of small-scale irregularities [Pi et al., 1997; Zakharenkova & Astafyeva, 2015]. It is calculated as a root-mean-square of the rate of TEC (ROT):

$$ROTI = \sqrt{<ROT^2> - <ROT>^2} \qquad (1)$$

where $ROT = \Delta I / \Delta t$, ΔI is the TEC change over time Δt, i.e. a temporal resolution of measurements (most typically 30 s). The ROTI is calculated over the 5-min time interval [Yasyukevich et al., 2020a; http://simurg.iszf.irk.ru]. To increase the resolution over Northern Eurasia (mostly the European part of Russia), we added data from the HIVE network (https://hive.geosystems.aero/).

3) **Density of TEC-slips** in data of ground-based GNSS-receivers [Astafyeva et al., 2014; Yasyukevich et al., 2018], was calculated as a number of sudden TEC jumps with respect to the total number of observations. Depending on latitude, the following changes in the slant TEC were regarded as TEC slips: 3 TECU per 30 s interval for low latitudes, 2 TECU/30 s for mid-latitudes (between ±25° and ±75° Lat) and 1TECU/30s for high latitudes (over ±75° of Lat). These estimations were done separately for GPS and Glonass observations.

4) **Precise point positioning (PPP) coordinates** in kinematic mode were calculated for GPS stations, by using the "GAMP" open source software [Zhou et al., 2018]. Receiver and satellite clock offsets were considered in GAMP PPP solution by applying IGS precise satellite orbit and clock products. The 24-hour averaged values of X, Y, Z coordinates for a station were regarded as reference positions. The total positioning error was calculated as a difference between the reference and the instant position:

$$\sigma_{XYZ} = \sqrt{(X^2 + Y^2 + Z^2)} \qquad (2)$$

5) **Doppler velocity of ionospheric scatters** as measured by the global network of high-frequency (HF)-radars SuperDARN. The SuperDARN is spread over the high

136 and mid latitude regions to study the ionospheric variability over a large scale

137 (Greenwald et al., 1995). Currently, the SuperDARN consists of total 36 radars, 23

138 in the northern hemisphere (NH) and 13 in the southern hemisphere (SH) [Nishitani

139 et al., 2019]. As known, field aligned ionospheric (FAI) disturbances of decameter

140 scale, generated over the polar and auroral regions, cause intensive HF

141 backscatter when the angle between HF wavevector and magnetic field is close

142 to perpendicular. Single HF radar is capable to measure Doppler velocity

143 component, which is primarily associated with the ExB plasma drift, along each

144 beam. To retrieve the full horizontal velocity vector intersection of several radars

145 beams is needed. However, observing the ionospheric scatter at a single beam,

146 one can conclude about the location of FAI generation regions and their dynamics.

147 In our study, we selected three meridional directions (60°E, 80°W, and 120°W) and

148 mapped ionospheric echoes observed by HF radars along these directions. To

149 study latitudinal expansion of auroral ionosphere convection during the

150 geomagnetic storm, we combined data from the polar cap, high-latitude, and mid-

151 latitude HF radars as was firstly shown by Baker et al. (2007). We used data from

152 six SuperDARN radars (and #beams) located in North America: Blackstone (bks

153 #18), Kapuskasing (kap #11), Rankin Inlet (rkn #6), Christmas Valley West (cvw

154 #18), Prince George (pgr #9), and Inuvik (inv #0). In addition, we also used data

155 from the Russian Ekaterinburg HF radar (ekb #1 and #2) whose characteristics are

156 similar to SuperDARN radars. To separate ionospheric echoes from the echoes of

157 other origin (i.e. ground scatter echoes) we apply a standard empirical criterion

158 [Blanchard et al., 2009]. Mapping is performed by using an empirical height model

159 developed by Chisham et al. (2008). We limited our analysis by echoes with power

160 greater than 6 dB.

161

162 **6) Vertical electron content (VEC)** calculated from measurements of GPS-receivers

163 onboard Swarm satellites. Similar to the ground-based GPS-receivers, the VEC

164 can be calculated from phase and code measurements, and by removing satellite

165 and receiver bias [e.g., Zakharenkova & Astafyeva, 2015]. The VEC reflects the

166 topside part of the VTEC, i.e. the part of VTEC above the satellites. In order to

167 assess the storm-time contribution, we remove the quiet-time reference level (for

168   24 August 2018) from the storm values. In order to avoid longitudinal and diurnal
169   artefacts, we perform orbit-by-orbit subtraction for all satellite data. The Swarm
170   constellation consists of three identical satellites: (A)lpha, (B)ravo and (C)harlie.
171   The Swarm A and C spacecrafts fly only several minutes and several degrees of
172   longitudes apart and, in most cases, show quite similar measurements. Here we
173   only use data from A and B (denoted below as SWA and SWB, respectively).
174   During the August 2018 storm, the orbital altitudes of the satellites were the
175   following: 430-460 km for SWA, 498 -525 km for SWB. The spacecrafts crossed
176   the equator at 2.5 & 14.5LT (SWA), and at 9.5 & 21.5LT (SWB).

178   **7) Space-borne Rate-of-TEC change Index (SROTI)** was calculated from VEC
179   data, similar to ROTI from ground-based GNSS-receivers [e.g., Zakharenkova et
180   al., 2016; Jin et al., 2019; 2020]. While the VEC data are 1s, for SROTI calculation,
181   we first estimate the median ROT for all GPS satellites with elevation higher than
182   30 degrees. The SROTI is a standard deviation of ROT over 10s running window.

184   **8) In-situ electron density (Ne)** measurements performed by two Langmuir Probes
185   onboard Swarm A and B. The Ne is the Swarm Level 1b product. In order to extract
186   storm-driven effects in the Ne, we calculate the dNe as the difference between the
187   storm-time and the quiet-time values. Similar to the dVEC data, this procedure is
188   done orbit-by-orbit for each satellite.

190   **9) In-situ electron density (Ne)** measurements performed by a Langmuir Probe
191   onboard the China Seismo-Electromagnetic Satellite (CSES, also known as
192   Zhangheng-1) [Shen et al., 2018]. The CSES was launched on 2 February 2018 on
193   a circular sun-synchronous orbit with inclination of 98° with descending node at
194   14LT and ascending node at 2LT. During the August 2018 storm, the orbital
195   altitude varied between 507 and 524 km. We note that the CSES local times are
196   close to those of SWA, and the CSES orbital altitude is close to the altitude of
197   SWB. Therefore, it is of interest to compare the measurements provided by the
198   two missions.

199   The Ne is Level 2 product, its sampling is 0.3 Hz. The issue is that the CSES

200   Langmuir Probe suffers from a systematic underestimation of the in-situ electron

201   density [Wang et al, 2019]. In addition, the Ne measurements often present spikes

202   and gaps in data (see example in Figure S1(a-b), supplementary material). All this

203   might compromise the general use of the Ne data. To overcome this problem, here

204   we propose a new method of data processing that allows to accurately extract the

205   storm effects in the CSES data. At the first step, we remove the spikes and we

206   smooth the raw Ne data with the centered running average procedure with 9-

207   second window (i.e., 3 consecutive values). Second, for the day and night side

208   passes separately, we estimate the quiet-time reference values based on data for

209   geomagnetically quiet days in August 2018: 1-12, 21-24 and 29-31. These

210   reference data are divided into cells, each of 2° of latitude and 2° of longitude. For

211   each cell, we compute the median value of the smoothed values from the previous

212   step. However, because of a large number of data gaps, some cells had no data,

213   therefore, for them we calculated the averaged value based on the data in 8

214   surrounding cells. The resulting reference maps for day and night sides are shown

215   in Figure S1c-f. Finally, at step 3, in order to estimate the storm-time contribution,

216   we first smoothed the storm-time data by averaging two consecutive values. Then,

217   we calculate the difference between the disturbed and quiet values, separately for

218   day and night passes. The final dNe values can be seen in Figure 3(a-b).

219

220 **10) Rate-of-Density Index (RODI)** was calculated from the Ne in-situ measurements

221   by the Swarm and CSES satellites. First, rate-of-Density (ROD) was calculated for

222   consecutive epochs similar to ROT. Second, RODI is calculated as the standard

223   deviation of ROD values in a centered running window of Δt, i.e. only ROD values

224   calculated between (t$-\Delta t/2$) and ($t+\Delta t/2$) are taken into account. Then, RODI at each

225   definite time *t* is:

226

$$RODI(t) = \sqrt{\frac{1}{N-1} \sum_{t_i = t - \frac{\Delta t}{2}}^{t + \frac{\Delta t}{2}} \left| ROD(t_i) - \underline{ROD}(t) \right|^2} \qquad (3)$$

227

228   *ROD(t$_i$)* are ROD values falling inside the window centered at time t and Δt= 30 s

229   wide for the CSES data and 10 s and 20 s wide for the Swarm data. N is the number

230   of ROD values, while $\underline{ROD}(t)$ is the mean of ROD values in the window. We note

231   that for the CSES data, because of a large number of spikes, we used the 3-pint

232   smoothed Ne data for RODI calculation.

233

234 **11) Field-Aligned Currents (FACs)** densities along the orbit of the Swarm satellites

235   [Lühr et al. 1996; 2015; Ritter et al., 2013] were analysed in order to understand

236   the location of the auroral region. FACs are present in the auroral zones at all local

237   time sectors and are flowing all the time although with highly variable intensity.

238   The FACs density is a Level-2 product, it is derived by the multiplication of the

239   radial current density with the inclination angle of the geomagnetic field [Swarm

240   handbook]. The uncertainty of FACs density estimation is 50 nA/m^2.

241

242 **12) Total electron density (Ne) and O+ fraction** as measured by the Defense

243   Meteorological Satellite Program (DMSP) at the altitude of 835 to 855 km. The

244   DMSP spacecrafts are placed in a near-circular, sun-synchronous, polar orbit with

245   inclination 98.8°–98.9° (http://dmsp.ngdc.noaa.gov). In this work, we use data

246   from DMSP F15 (equatorial crossings at 14.9LT and 2.9LT), F16 (15.9LT and

247   3.9LT), F17 (6.6 and 18.6LT) and F18 (5.9 and 17.9LT). In addition, we use the

248   Google EDR (Environmental Data Records) Auroral product based on DMSP

249   measurements by the Special Sensor Ultraviolet Spectrographic Imager (SSUSI)

250   instrument and a fitted GUVI (Global UltraViolet Imager) model global boundary

251   [Paxton et al., 2018].

252

253

254 **3. 25-26 August 2018 Geomagnetic Storm**

255   The storm was caused by a Coronal Mass Ejection (CME) that left the Sun on

256 20 August, and reached the Earth at 2:45UT on 25 August [Piersanti et al., 2020;

257 Blagoveshchensky and Sergeeva, 2019]. The initial phase began at ~7:45UT (Figure

258 1). At 17UT, the south-north component of the interplanetary magnetic field (IMF Bz)

259 turned negative and intensified to –17 nT (Figure 1a). The IMF Bz further remained

260 unchangeably negative until ~10UT of the next day, when it returned to zero level for

261 a brief moment of time. Between ~10 and ~21UT the IMF Bz showed several large-
262 amplitude fluctuations.

263   The SYM-H index started to gradually descend from ~17.5UT on 25 August (Figure
264 1c). From ~20 to ~22.5UT it remained at a "plateau" level of about –28-30 nT, and
265 from ~23UT, the SYM-H dropped faster and reached the minimum of –207 nT at 5UT
266 on 26 August. From ~7UT, the SYM-H index began to slowly grow up but remained
267 below zero until 31 August 2018. From the point of view of the minimum SYM-H
268 excursion, this storm has become the third strongest in the 24th solar cycle.

269   The storm of 25-26 August was accompanied by enhanced substorm activity.
270 Variations of the auroral electrojet (AE) index are shown in Figure 1d. It should be
271 pointed out that those are preliminary data from the World Data Center for
272 Geomagnetism in Kyoto (WDC-Kyoto, http://wdc.kugi.kyoto-u.ac.jp/) and might
273 contain some errors. The provisional data sets are not yet available. Figure 1c shows
274 that the AE index started to grow gradually from 16UT on 25 August and went up to
275 1000 nT by 19.3-23UT. The maximum of ~2200 nT was reached at 7.5-8.5UT on 26
276 August 2018, i.e., early recovery phase of the storm. One can also see three other AE
277 peaks of ~1,000-1,500nT during the day: at 11-13, 15-17, and 20-20:30UT.

278

279

280 **4. Results & Discussions**

281   In this work, we will focus on the time period from 17UT on 25 August to 10UT on
282 26 August 2018. This corresponds to the main phase (17UT – 7UT) and early recovery
283 phase (7-10UT) of the storm. The full picture of the ionospheric storm-time changes
284 during the 2 days of the event, including time before the main phase and the recovery
285 phase, can be understood from Animations S1 and S2 (available as supplementary
286 material), and from satellites observations SWA, CSES and SWB (Figures 2, 3, and 4,
287 respectively, and Figures S2 and S3). Animations S1 and S2 also present the evolution
288 of indices ROTI (from ground-based GNSS) and RODI/SROTI (from space-borne data)
289 during the two days of the storm.

290   The key features of the development of the ionospheric storm on 25-26 August
291 2018 are presented in the VTEC in Figure 5. One can see that at different stages of
292 the storm, numerous large- and small-scale ionospheric increases and decreases

(referred to as positive and negative ionospheric storms, respectively) occurred throughout the world.

4.1. Ionospheric effects in Atlantic-European-African region

At the very beginning of the storm, over South America and the Atlantic Ocean, at low latitudes negative VTEC disturbance of a ~8-10 TECU occurred (Figure 5a,b; Animation S1). While, on the west coast of South America one can see a VTEC enhancement of 12-15 TECU. Such a difference in the observed effects could be explained by different directions of the equatorial electric fields and the EEJ on the east and west coasts [Spogli et al., 2021]. With the development of storm, these positive and negative low-latitude effects persist and become reinforced. From ~19:00UT, the negative effect drops by -5-7 TECU below the quiet-time reference level, and it further extends to post-sunset sector (over Africa), while the dVTEC/VTEC enhancement extends to the Pacific region (Animation S1; Figures 5a,b). More details on the development of the ionospheric storm in the Pacific and American regions can be found in Sections 4.4 and 4.5 below.

Over North Africa (around 30N), from 20:20UT we observe ~8-10 TECU increase in the dVTEC (Figure 5b). This enhancement first occurred in the local post-sunset hours and further reinforced and persisted until late local night hours (Figure 5c-e; Animation S1). The observed effect was asymmetric with respect to the magnetic equator, as in the southern hemisphere the low-latitude increase is much smaller. Satellite observations confirm the occurrence of the hemispherically asymmetric enhancement during their passages over this sector. The effect is seen at ~22-22.7UT on 25 August dVEC data of SWB (Figure 4b), and at ~1.5-3.5UT on 26 August in the dNe data of SWA (Figure 2c) and CSES (Figure 3b). The observed enhancement was, most likely, partly induced by a combination of the pre-reversal enhancement of zonal electric fields and of the storm-time prompt penetration electric fields that often affects the post-sunset sector (e.g., Kikuchi et al., 2016), by uplifting the ionospheric plasma to higher altitudes where the recombination time is longer. However, it is not yet clear how the ionization increases without solar irradiance (e.g., Astafyeva et al, 2015a). The observed asymmetry of the ionospheric response should be due to the impact of thermospheric winds and seasonal effects.

325   One can also note the occurrence of rapid intensive fluctuations in the Ne along
326   with increase in RODI and SROTI indices over this particular region (Animation S2,
327   SWA data). Ground-based ROTI also depicts this disturbance area although of
328   seemingly smaller magnitude (Animation S1). Ionospheric irregularities often occur in
329   a post-sunset sector driven by generalized Rayleigh-Taylor instability (e.g., Kelley et
330   al., 2011).

331   In North Eurasia, along ~60-70N of latitude, from ~20:50 UT, we notice ~8-12
332   TECU increase in dVTEC. This enhancement occurred around the high-latitude
333   boundary of the solar terminator. It is extended over several tens of degrees in
334   longitude (local midnight to local early morning hours), and, with time, it follows the
335   solar terminator (Figures 5b-e, Animation S1). This enhancement can also be seen in
336   the night-side Ne data of SWA, reaching ~$1*10^5$ cm^{-3} (Figure 2c). However, it was not
337   captured by either CSES (the same LT but higher altitudes) or SWB (higher altitudes
338   and different LT) (Figures 3 and 4). Further analysis shows that the position of this
339   positive effect coincides with the area of the intensive FACs, as measured by both
340   SWA and SWB when passing over this region (Animation S2). One can also notice an
341   increase in the RODI and SROTI in satellite data. Therefore, one can suspect the
342   correlation between this region with enhanced TEC and the auroral region. Indeed,
343   Figure 6a-b confirms that the dVTEC enhancement and the region of the intensified
344   ROTI are located between the equatorward and poleward boundaries of the auroral
345   oval. This conclusion can also be confirmed by the data from the EKB radar (Figures
346   6c), that shows intensive ionospheric scatter between ~21:30 and 23:30 along the
347   same latitudinal interval as the intensive FACs and ROTI.

348

349

350   **4.2.   Ionospheric effects in Asian-Australian region**

351   In Asian-Australian sector (between 60 and 180°E), positive storm effects in
352   GNSS-derived VTEC are first seen at ~23UT on 25 August (Figure 5c-d, Animation
353   S1). This dayside effect was at first hemispherically asymmetric, the maximum storm-
354   time VTEC contribution reached 5-10 TECU over North Australia. While, in the NH,
355   the dVTEC did not exceed 3-4 TECU. This asymmetry was observed until ~4UT. From
356   ~4:40UT, the dayside positive storm became more symmetric (Figure 5f). This

enhancement is the strongest observed during this storm, it exceeded 15 TECU over to the quiet-time level and reached 50 TECU in absolute VTEC (Figure 7). The satellite observations also suggest strong storm-time changes in both in-situ electron density and the topside VEC (Figures 2-4; Figures S2 and S3). First, SWB flew over this region between 21.9 UT and 5.8UT (~9.5LT sector, Figure 4c,d; S3c,d). During this time, the dNe in the NH was very little disturbed, while in the SH at low latitudes a small enhancement of ~1-2*10^5 cm^{-3} was observed (i.e., 100-200% with respect to the quiet time). This hemispheric asymmetry is in line with GPS-derived dVTEC observations. However, the topside VEC shows quite different pattern. From Figure 4d, one can see that the storm-time VEC deviation is hemispherically symmetric. Also, the low-latitude VEC was more disturbed than the in-situ Ne, and the response was much more symmetric. The storm-time VEC exceeded the quiet-time reference value by 3-6TECU, which represents ~100% increase as compared to the quiet-time values (Figures 4d and S3d). One can also notice that the in-situ Ne values over the magnetic equator at ~23.5, 1.09 and 2.66UT were smaller than during the quiet-time (Figures 4c, S3c). The concurrent VEC measurements confirm the occurrence of the ionospheric depletion over the magnetic equator (Figure 4d). Therefore, we conclude that the observed effects in the Ne and VEC were due to the storm-time reinforcement of the EIA, also known as the dayside super-fountain effect (SFE, e.g., Tsurutani et al., 2004; Mannucci et al., 2005; Astafyeva, 2009). Our conclusions are in line with results presented by Bolaji et al (2021), who showed an extreme increase of the intensity of the horizontal magnetic field, and, consequently, the enhancement of the ExB drift in this region.

The SWA and CSES spacecrafts passed over the West Pacific and Asian sector between ~4 to ~9 UT on 26 August (Figures 2a-b; 3a-b; S1b; S2a-b; 7), i.e. during the most significant ionospheric effects occurred due to this storm. Both spacecrafts showed more symmetric increase in both Ne and VEC, at low and middle latitudes than at earlier hours. At 5-7UT, in the Ne data, one can clearly notice the occurrence of 2 large peaks of ionization (the crests of the EIA) with increased distance between them at ~6.98 (CSES) and ~7.37UT (SWA). The storm-time increase in the Ne represents 300-500% increase with respect to the quiet-time levels (Figure 7). In the VEC data, we observe a drastic increase of more than 12 TECU over the equatorial

389   and low-latitudes at ~5.81UT and 7.37UT (Figure 2b). Figure 7 shows that the topside

390   TEC at low latitudes and mid-latitudes in the NH increased by 70-100% as compared

391   to the quiet-time reference values. Also, it should be noted that the topside VEC

392   represents about a half of the total VTEC as seen from Figure 7. Such observations

393   indicate the ionospheric uplift over this region during this period of time, driven by the

394   enhanced equatorial ExB drift. Indeed, the in-situ Ne measurements made by the

395   DMSP satellites F15 and F16 at the altitude of ~850km confirm that during the

396   strongest ionospheric enhancement, the topside Ne significantly increased over the

397   equator (Figure 7). Further comparison of Animations S1 and S2 reveals that no ROTI

398   and SROTI/RODI fluctuations during this time in the Asian region.

399

400

401   **4.3.   Ionospheric effects in Pacific region**

402   Over the Pacific Ocean (180°W–120°W), a huge positive storm in VTEC/dVTEC

403   can be seen by GNSS-receivers located on islands starting from ~18:30UT (Animation

404   S1; Figure 5a-d). This dayside ionospheric storm was much stronger in the NH, with

405   the dVTEC exceeded the quiet-time levels by ~15TECU and reached 50 TECU in

406   absolute values. The in-situ Ne observations made by SWA during the dayside passes

407   (~14.5LT) confirm that the storm-time increase was much stronger in the NH (Figures

408   2a and S2a, passes between 22.03 and 1.14UT). The CSES flew in the same LT region

409   and showed quite similar results (Figure 3a).

410   The observed enhancement diminished by ~3:30UT (local evening hours),

411   however, with the arrival of the solar terminator, from ~5:10UT, both the VTEC and

412   dVTEC strongly increased along ±20-25°N (Animation S1, Figures 5f,g). While,

413   equatorward from these enhancements, the dVTEC dropped. SWB measurements in

414   the ~21.5LT sector confirm the strong storm-time increase at low latitudes in both Ne

415   and VEC (Figures 4a-b, S3a-b), as well as the depletion over the magnetic equator

416   (Figure 4a, passes at 6.61 and 8.19UT). The observed signatures resemble the SFE,

417   however, we note that we observe such effects in the post-sunset sector (~19-22LT).

418   The post-sunset SFE is often observed during geomagnetic storms driven by a

419   combination of the "regular" pre-reversal enhancement of ExB drift and the storm-

420   time penetration of the eastward electric fields that can extend up to ~22-23LT [e.g.,

421 Kikuchi et al., 2008; 2016]. We note, however, that the physical mechanism of the

422 night-time ionization increase within the SFE is not well explained yet [e.g., Astafyeva

423 et al., 2015a].

424   DMSP F17 satellite measurements show that the increase in the electron density

425 reaching as high as ~850 km of altitude (Figure 9a). Concurrently, a very strong

426 enhancement of the O+ fraction over the Ocean at 5.45 –7.15UT, confirming the

427 ionospheric uplift at the magnetic equator by the ExB drift [e.g., Tsurutani et al., 2006].

428   During this period of time, we notice strong fluctuations of ground-based ROTI

429 (Animation S1), that persist throughout the night until ~11:30UT. SWB also showed

430 very strong fluctuations of the electron density over the Pacific Ocean (Figures 4a,

431 S3a, 9b). The space indices SROTI and RODI showed quite dramatic values: RODI

432 reached 70-80 cm-^{3}/s while SROTI exceeded 0.12TECU/s at 8.2UT on 26 August

433 (Figure 9b). Those are the highest values observed during this storm, and they are

434 ~10-50 times higher than those observed over the auroral areas. These fluctuations

435 seemed to persist in this region until at least ~11-12UT (SWA measurements in 2.4LT),

436 although their intensity diminished (Figure 9c). These observations are in line with the

437 ground-based ROTI results.

438

439

440 **4.4.   Ionospheric effects in American Sector**

441   The storm effects were the most complex in the American sector. Partly they were

442 discussed in previous works [Astafyeva et al., 2020; Spogli et al., 2021]. Here we

443 particularly focus on the ionospheric storm effects between 17UT on 25 August and

444 10UT on 26 August, and we first discuss storm-time changes over North America.

445   At the beginning of the storm, the dVTEC over the West coast and the Pacific

446 Ocean exceeded the quiet-time values by 15 TECU, reaching ~32TECU in absolute

447 VTEC (Figure 5a; Animation S1). Further, this enhancement extended toward mid-

448 latitudes and merged with the high-latitude storm-time dVTEC enhancement of ~4-7

449 TECU (Figure 5b). The most pronounced effects occurred between ~22:30 on 25

450 August and 01:00UT on 26 August (Figure 5c,d and Animation S1). We observe very

451 significant positive storm signatures, with the maximum storm-time dVTEC

452 enhancement over 15 TECU at low latitudes and over the West coast of North

453   America. Both SWB and DMSP data are in line with dVTEC observations and confirm

454   ionospheric positive storm over low-latitudes (Figure 8). The DMSP data also show a

455   significant increase in the O+ fraction over the equator with respect to the quiet day,

456   indicating the ionospheric uplift that was, most likely, driven by a combination of the

457   pre-reversal enhancement and the storm-time penetration of the eastward electric

458   field.

459   At high latitudes (above +60°N), we see a depletion of about -2-3TECU in dVTEC

460   and very low TEC values in the absolute VTEC. This band-like depletion was

461   elongated through the entire North American continent, and should be due to the mid-

462   latitude ionospheric trough (MIT; Moffett et al., 1983; Karpachev et al, 2016; Aa et al.,

463   2020). The MIT signatures are also seen in the Ne measured by Swarm B (Figure 8).

464   DMSP measurements show that the O+ fraction drops around the MIT, confirming the

465   link to the trough (Moffett et al, 1983). With the arrival of the solar terminator into this

466   region, from 00:20UT on 26 August, the depletion descends to 42-45°N and expands

467   in latitude on the east coast of the USA, and the absolute VTEC decreases to 20-30

468   TECU. This post-sunset expansion of the depletion can be explained by sub-auroral

469   polarization stream (SAPS) heating the plasma and increasing the loss rates [Fuller-

470   Rowell, 2011].

471   Below the depletion, at mid-latitudes and between 100°W and 120°W of

472   longitude), from 01:25 to 02:40UT, we observe an elongated plume-like enhancement

473   of ~5-8TECU (Animation S1, Figure 5e), which resembles a storm-enhanced density

474   (SED)-plume [Foster, 1993; Foster et al., 2005; Valladares et al., 2017]. The SED

475   plumes occur as a result of the equatorward motion of high-latitude convection

476   electric field (the SAPS) that transport high-density plasma from lower latitudes

477   toward the cusp, sometimes forming a tongue of ionization (TOI) in the polar region

478   [Foster, 1993; Thomas et al., 2013; Zou et al., 2014; Foster et al., 2021]. During the

479   August 2018 storm, the TOI was not formed, however, the SED-plume was clearly

480   visible in the dVTEC/VTEC data during several hours (from ~1UT to ~3:25UT).

481   SuperDARN data confirm the presence of high-speed flows on the south from the

482   equatorward boundary of the auroral oval during the SED observation time (Figure

483   S4). Animations S1 and S2 show that the high ionization within the SED-plume

484   seemed to be initially produced by particle precipitation at high-latitude (Animation

485 S1, ~18:50-20UT). With the storm development, additional ionization was transported
486 from low-latitudes to high-latitudes (~20:30-21:40UT). The concurrent SWA pass
487 showed a drastic increase in the topside VEC at high-latitudes (Figure 2b, pass with
488 equatorial crossing at 22.03UT). Further, the dVTEC equatorward from the plume
489 diminished (00:15-02:20UT), while the ionization within the plume persisted until
490 ~03:25UT.

491 The SED-plume enhancement is also clearly visible in the in-situ DMSP Ne
492 measurements, indicating that the feature went upward to at least ~840 km (Figure
493 8). Such altitudinal extent is in line with previous observations (e.g., Foster et al.,
494 2021). Unfortunately, DMSP ion drift data were not of sufficient quality to be helpful
495 for our analysis. The SED and SED-plumes are known to be associated with
496 significantly elevated electron densities, low electron temperatures, and large
497 convection flows [Foster et al., 2005; Zou et al., 2014], and with high electron density
498 and TEC gradients [Foster and Rideout, 2005; Zou et al., 2013; Zakharenkova and
499 Cherniak, 2020; Nishimura et al., 2021]. In our case, the SED-plume was of moderate
500 amplitude and was not associated with irregularities as shown below.

501 From ~02:30UT, one can notice a small-amplitude dVTEC increase at ~50-55°N
502 (Animation S1 and S2). The latter elongated feature is clearly seen in the data of the
503 absolute VTEC as well. Similar to the depletion, the enhancement persisted
504 throughout the night-time hours and was visible over the North America until ~9:30-
505 10UT (Animation S1). The enhancement was the most pronounced at 7:20-7:25UT.
506 Figure 8 shows that this high-latitude dVTEC enhancement is located between the
507 two boundaries of the auroral oval.

508 In South America, the initial small negative VTEC ionospheric storm at low-
509 latitudes (between ~19:40 and ~22:30UT) was followed by a small positive storm of
510 ~2-4 TECU that persisted for several hours. A very particular feature can be seen in
511 both VTEC and dVTEC over the equatorial and low-latitude region from ~1:40 to 4UT
512 (Animation S1, Figure 8; Figure S5). We clearly notice several stripe-like increases and
513 decreases in the dVTEC that are extended in latitude and are perpendicular to the
514 magnetic equator. We consider these structures to be the representation of equatorial
515 plasma bubbles (Valladares et al., 2006; Takahashi et al., 2015; Zakharenkova et al.,
516 2019). The closest SWB pass (equator time crossing at 3.45UT) showed very

significant fluctuations in the electron density (Figures 8, 4a, S3a). The Jicamarca ionosonde station showed strong Equatorial Spread-F (ESF) signatures during the considered period of time (Figure S5). We point out that the bubbles are not seen in ROTI data (Animation S1 and Figure S5).

4.5. Ionospheric Irregularities and their effects on GPS-based navigation. Relation to the auroral region

The global values of TEC-slips for GPS (G) and Glonass (R) observations are shown in Figure 1e and 1f, respectively (black lines). The dynamics of G-TEC-slips follows the development of the storm. The number of slips starts to increase with the beginning of the storm at ~17UT, it reaches the maximum value of 1% by 5-6UT on 26 August, and descends slowly to undisturbed value at the end of the day. Such global values of TEC-slips are comparable with other intensive storms but are below effects caused by super-storms, such as that of 20 November 2003 and 15 May 2005 when the global value of TEC-slips reached 4-9% (Astafyeva et al., 2014). Separation into latitudinal sectors shows that the vast majority of GPS-slips occurs at high-latitudes. In G-TEC-slips, the value reached 3.4% by 5UT on 26 August. By the end of the main phase of the storm, the high-latitude slip level further diminishes, however, it rises again to 2,2% during the recovery phase (9-12UT).

The level of low-latitude slips remains low during this storm, while, the TEC-slips at mid-latitudes reach 1% at 6-7UT on 26 August. The latter is, undoubtedly, caused by the descent of the auroral area from high-latitudes into mid-latitudes, over the American sector, as discussed previously.

The global percentage of TEC-slips in Glonass observations shows different behaviour: it increases up to 0.8% during the storm, and we observe a spike of ~2.2% before the storm. The latter is, most likely, related to very few high-latitude observation points in Glonass measurements. Similar to GPS-TEC-Slips, the majority of slips were observed at high-latitudes, and an increase was seen at 3-7UT on 26 August in mid-latitude slips. Also, the rate of high-latitude R-slips increases up to 1.5% during the recovery phase (13-14UT on 26 August).

548   The global evolution and distribution of ionospheric irregularities with a particular

549   focus on high-latitude regions can be seen from Animation S2 (supporting material).

550   One can see that before the storm the ground-based ROTI remained very low, with

551   only increases up to 0.3-0.7TECU/min in the vicinity of the magnetic poles in both

552   hemispheres. In the northern hemisphere, this disturbed area is confined within 20

553   degrees of latitude on the dayside. Several singular increases are seen over North

554   America. No storm-time deviations are observed in dVTEC. Satellite observations

555   show low values of the ionospheric parameters (Ne and VEC), and SROTI is below

556   0.02-0.03 TECU/s and RODI does not exceed $5*10^3$ cm^{-3}/s. With the development of

557   the storm, the high-latitude ROTI in the NH increases, and extends to the night-side

558   as well, forming a circle. From ~17:50UT, this disturbed area starts to extend in

559   latitudes. In the SH, due to the limited number of GNSS stations, the picture is less

560   evident. One can only notice the increase of the ROTI over Antarctica and close to the

561   magnetic pole. From ~19:15UT, the SROTI and RODI from SWA data increases while

562   the spacecraft passes over high-latitude region in SH. We notice that these

563   enhancements coincide with the areas of intensive FACs (Animation S2), confirming

564   the close vicinity to the auroral oval region (e.g., Xiong et al, 2014; Jin et al. 2019;

565   2020). Similar pattern is observed during the SWA passage over the NH high-latitude

566   region ~45 min later. We note that the "auroral" areas depicted by the SWA satellite

567   corresponds quite well to the regions of the enhanced ROTI. The SROTI and RODI

568   indices from SWB are lower than that at SWA, and the FACs seem less intensive.

569   Nevertheless, they allow to image the disturbed areas and are as well in line with

570   ground-based ROTI. As for the CSES results, there is a systematic data gaps over the

571   geographic poles (above ±80°), which might make it difficult to use these data for

572   "imaging" of the polar regions. However, in the data below the "blank regions", the

573   increases in the CSES-RODI also correspond to the enhanced ROTI areas in both

574   hemispheres.

575   As the storm progresses, in the NH we observe gradual expansion of the

576   disturbed ROTI region, it is especially noticeable starting from ~1UT on 26 August and

577   on. At 7:25UT (i.e. 25 min after the beginning of the recovery phase) the region of the

578   enhanced ROTI has the maximum amplitude and the largest extension in latitude (10-

579   30 degrees). The disturbance is stronger on the night side, and it descends down to

580   42-45N of geographic latitude in North America, which corresponds to the position of
581   the equatorward boundary of the auroral oval (Figures 6e,h and 10). This descent
582   should be the cause of the significant increase of the mid-latitude TEC-slips as
583   discussed previously (Figure 1e-f). Starting from ~8:20UT, this region starts to go back
584   poleward, and it becomes less intensive, which is in line with the auroral oval
585   development. Overall, our results show good agreement between the ROTI and the
586   storm-time evolution of the equatorward and poleward boundaries of the auroral oval
587   (red curves in Figure 6). The auroral region and the boundaries of the auroral oval are
588   known to be the source of intensive irregularities because of steep Ne gradients
589   occurring in these regions due to significant particle precipitation and FACs from the
590   magnetosphere, which provide free energy for the development of ionospheric
591   irregularities [e.g., Afraimovich et al., 2004; 2009; Cherniak and Zakharenkova, 2016;
592   Jin et al., 2019; 2020; Zakharenkova & Cherniak, 2020; Yasyukevich et al., 2020b;
593   Nishimura et al., 2021]. In our results, we see ROTI disturbance not only at the
594   boundaries, but also inside the whole auroral region. Moreover, our results
595   demonstrate that at least in the NH the ground-based ROTI maps can serve an
596   indicator of the storm-time evolution of the auroral region. It is especially interesting
597   knowing that it is possible to obtain ROTI maps with 30-sec time resolution. We note
598   that during the August 2018 storm the ground-based ROTI was also disturbed in polar
599   regions, while it was less obvious in the space-based SROTI/RODI indices. The latter
600   could indicate that the polar irregularities occur at lower altitudes, or that they are
601   short-lived in time, so that the satellites do not capture many of them. In the polar
602   region, polar patches and other rapid changes in the electron density can be the
603   source of irregularities (Xiong et al., 2019; Jin et al., 2019; 2020).

604   The storm-time evolution of ionospheric irregularities in the SH is more difficult
605   to follow. Animation S2 and Figure 11 show that the space-borne indications of the
606   auroral area partly correspond to the increases of the ground-based ROTI. While, over
607   the oceans, we can only rely on space-based observations in order to further
608   investigate the dynamics of the irregularities. We note that in general the SROTI and
609   RODI indices are higher in the SH than in the NH (Animation S2). The largest
610   expansion of the disturbance area was observed at 7:00-7:40UT, which is similar to

611 the NH. This is most likely related to the intensification of the AE during this period of

612 time and to particle precipitation (Figure 1c).

613   One can notice that, throughout the storm, the ROTI disturbance does not

614 always correspond to dVTEC increase. However, the significant storm-time

615 enhancement that was observed at low and mid-latitudes at 2-5UT on 26 August is

616 associated with ROTI fluctuations (Figure 6g and 6h). Ionospheric scatter dynamics

617 as seen by SuperDARN HF radars in North America show very similar temporal

618 behaviour (Figures 6f,i) as dVTEC and ROTI. The differences in latitudinal filling might

619 be addressed to radar limited field-of-view and HF propagation conditions.

620   The impact on the GPS-based navigation can be seen in PPP (Figures 10, 11

621 and S6). One can see that the largest errors (up to 0.5 m) occur in the auroral region

622 at the end of the main phase of the storm, and beginning of the recovery phase. In

623 addition to high-latitude regions, we notice 0.2-0.3m errors at mid-latitudes in both

624 hemispheres. They are especially visible in North and South America and in Europe.

625

626

627   **5. Summary and Conclusions**

628   Our multi-instrumental analysis allowed to investigate in detail the generation

629 and evolution of large- and small-scale ionospheric disturbances during the 25-26

630 August 2018 geomagnetic storm. The most significant 100-300% large-scale

631 enhancement occurred over the Asian region between ~2 and ~8 UT on 26 August

632 (i.e., at the end of the main phase and beginning of the recovery phase of the storm),

633 driven by the storm-enhanced equatorial ExB drift.

634   The most complex effects were observed in the American sector. At the

635 beginning of the storm, TEC and Ne enhancements occurred over North America at

636 low and high latitudes, caused by the storm-time reinforcement of the EIA at low

637 latitudes and by particle precipitation at high latitudes. With the arrival of the night-

638 time, we observed a series of smaller-scale positive and negative ionospheric

639 disturbances at middle and high latitudes that were attributed to a SED-plume, MIT

640 and auroral oval. In South America, VTEC and dVTEC data clearly showed the

641 occurrence of the plasma bubbles. However, ROTI index did not increase around the

642 bubble area nor above the SED-plume. Only low- and partly mid-latitude

643 enhancement on the south-west of North America, that occurred during the night-
644 time hours, is seen in the ROTI data.

645   The storm also produced significant ionospheric irregularities in the auroral
646 region in both hemispheres. However, much stronger fluctuations occurred over the
647 Pacific Ocean at low and middle latitudes.

648   Overall, we conclude that observations by SWA, SWB and CSES are in
649 agreement with the observations performed by the ground-based GPS receivers,
650 although they mostly represent the topside disturbances and irregularities. Our
651 method suggested here demonstrates that CSES Ne measurements can be used to
652 study ionospheric effects of geomagnetic storms. Also, CSES-RODI can provide
653 information about the distribution of ionospheric irregularities. However, the CSES LP
654 instrument seems to be less sensitive and does not capture smaller changes in the
655 electron density, that, consequently, might impact the CSES-RODI data.

656
657

704

705   **References**

Aa, E., Zou, S., Erickson, P. J., Zhang, S.-R., & Liu, S. (2020). Statistical analysis of the main ionospheric trough using Swarm in situ measurements. *Journal of Geophysical Research: Space Physics*, 125, e2019JA027583. DOI:10.1029/2019JA027583

Afraimovich, E.L., E.I. Astafyeva, V.V. Demyanov, I.F. Gamayunov. (2009) Mid-Latitude Amplitude Scintillation of GPS Signals and GPS Performance Slips. *Adv. Space Research*, V.43, No. 6, 964-972, doi:10.1016/j.asr.2008.09.015.

Afraimovich, E.L., Astafieva E.I., Berngardt O.I., Lesyuta O.S., Demyanov V.V., Kondakova T.N., and Shpynev B.G. (2004) Mid-latitude amplitude scintillation of GPS signals and GPS performance slips at the auroral oval boundary. *Radiophysics and Quantum Electronics*, v.47, N7, 453-468.

Astafyeva, E.I. (2009) Dayside ionospheric uplift during strong geomagnetic storms as detected by the CHAMP, SAC-C, TOPEX and Jason-1 satellites. *Advances in Space Research*, 43, 1749-1756, doi:10.1016/j.asr.2008.09.036.

Astafyeva, E., E.L. Afraimovich, E.A. Kosogorov (2007) Dynamics of total electron content distribution during strong geomagnetic storms, *Advances in Space Research*, V.39, 1313-1317, doi:10.1016/j.asr.2007.03.006.

Astafyeva, E., Yu. Yasukevich, A. Maksikov, I. Zhivetiev. (2014) Geomagnetic storms, super-storms and their impact on GPS-based navigation. *Space Weather*, V.12, 508-525, doi:10.1002/2014SW001072.

Astafyeva, E., I. Zakharenkova and E. Doornbos. (2015a) Opposite hemispheric asymmetries during the ionospheric storm of 29-31 August 2004. *J. Geophys. Res. - Space Physics*, V.120, N1, 697-714, doi:10.1002/2014JA020710.

Astafyeva, E., I. Zakharenkova, and M. Förster. (2015b) Ionospheric response to the 2015 St. Patrick's Day storm: a global multi-instrumental overview. *J. Geophys. Res. Space Physics*, V.120, N10, 9023-9037, doi:10.1002/2015JA021629.

Astafyeva, E., I. Zakharenkova and P. Alken. (2016a) Prompt penetration electric fields and the extreme topside ionospheric response to the 22-23 June 2015 geomagnetic storm as seen by the Swarm constellation. *Earth Planets and Space,* V.68, doi:10.1186/s40623-016-0526-x.

Astafyeva, E., I. Zakharenkova, and Y. Pineau. (2016b) Occurrence of the dayside three-peak density structure in the F2- and the topside ionosphere. *J. Geophys. Res. - Space Physics*, V.121, N7, 6936-6949, doi:10.1002/2016JA022641

Astafyeva, E., M.S. Bagiya, M. Förster, N. Nishitani. (2020) Unprecedented hemispheric asymmetries during a surprise ionospheric storm: a game of drivers. *J. Geophys. Res. - Space Physics*, V. 125, N3, doi:10.1029/2019JA02726

Baker, J. B. H., R. A. Greenwald, J. M. Ruohoniemi, K. Oksavik, J. W. Gjerloev, L. J. Paxton, and M. R. Hairston (2007), Observations of ionospheric convection from the Wallops SuperDARN radar at middle latitudes, J. Geophys. Res., 112, A01303, doi:10.1029/2006JA011982.

746 Blagoveshchensky, D. V. and M. A. Sergeeva (2019) Ionospheric parameters in the
747   European sector during the magnetic storm of August 25–26, 2018. *Advances in*
748   *Space Research*, doi:10.1016/j.asr.2019.07.044.
749 Blanchard GT, Sundeen S, Baker KB (2009) Probabilistic identification of high-
750   frequency radar backscatter from the ground and ionosphere based on spectral
751   characteristics. Rad Sci 44:RS5012. doi:10.1029/2009RS004141.
752 Bolaji, O. S., Fashae, J. B., Adebiyi, S. J., Owolabi, C., Adebesin, B. O., Kaka, R. O.,
753   et al. (2021). Storm time effects on latitudinal distribution of ionospheric TEC in the
754   American and Asian-Australian sectors: August 25–26, 2018 geomagnetic storm.
755   *Journal of Geophysical Research: Space Physics*, 126, e2020JA029068. Doi:
756   10.1029/2020JA029068
757 Cherniak I, Zakharenkova I (2016) High-latitude ionospheric irregularities: differences
758   between ground- and space-based GPS measurements during the St. Patrick's
759   Day storm. *Earth Planets Space*, 68, 136, doi:10.1186/s40623-016-0506-1.
760 Cherniak I, Zakharenkova I, Sokolovsky, S. (2018) Multi-instrumental observation of
761   storm-induced ionospheric plasma bubbles at equatorial and middle latitudes.
762   *Journal of Geophysical Research: Space Physics*, 124(3), 1491–1508.
763   https://doi.org/10.1029/2018JA026309
764 Chisham, G., Yeoman, T. K., and Sofko, G. J.: (2008) Mapping ionospheric
765   backscatter measured by the SuperDARN HF radars – Part 1: A new empirical
766   virtual height model, Ann. Geophys., 26, 823–841, https://doi.org/10.5194/angeo-
767   26-823-2008.
768 Demyanov, V.V., Yu.V. Yasukevich, A.B. Ishin, E.I. Astafyeva. (2012) Ionospheric
769   super-bubble effects on the GPS positioning relative to the orientation of signal
770   path and geomagnetic field direction. *GPS solutions*, V.16, N2, 181-189,
771   doi:10.1007/s10291-011-0217-9.
772 Dow, J.M., Neilan, R.E. & Rizos, C. (2009) The International GNSS Service in a
773   changing landscape of Global Navigation Satellite Systems. J Geod 83, 191–198.
774   https://doi.org/10.1007/s00190-008-0300-3
775 Foster, J. C. (1993). Storm time plasma transport at middle and high latitudes. *Journal*
776   *of Geophysical Research*, 98, 1675– 1689. https://doi.org/10.1029/92JA02032
777 Foster, J. C., and W. Rideout (2005), Mid-latitude TEC enhancements during the
778   October 2003 superstorm, *Geophys. Res. Lett.*, 32, L12S04,
779   doi:10.1029/2004GL021719.
780 Foster, J. C., & Coster, A. J. (2007). Conjugate localized enhancement of total electron
781   content at low latitudes in the American sector. *J. Atmos. and Solar-Terrestrial*
782   *Physics*, 69(10–11), 1241–1252. https://doi.org/10.1016/j.jastp.2006.09.012
783 Foster, J.C., S. Zou, R. A. Heelis, and P. J. Erickson (2021) Ionospheric Storm-
784   Enhanced Density Plumes. *Space Physics and Aeronomy Collection, Volume 3:*
785   *Ionosphere Dynamics and Applications, Geophysical Monograph 260, First Edition*
786   *Edited by Chaosong Huang and Gang Lu,* American Geophysical Union. Published
787   2021 by John Wiley & Sons, Inc. DOI: 10.1002/9781119815617.ch6

Fuller-Rowell, T. J. (2011). Storm-time response of the thermosphere-ionosphere system. In M. A. Abdu, D. Pancheva, & A. Bhattacharyya (Eds.), Aeronomy of the Earth's Atmosphere and Ionosphere, IAGA Spec. Sopron Book Ser, (Vol. 2, chapt. 32, pp. 419–435). Dordrecht, Netherlands: Springer. https://doi.org/10.1007/20978-94-007-0326-1

Greenwald, R. A., Baker, K. B., Dudeney, J. R., Pinnock, M., Jones, T. B., Thomas, E. C., et al. (1995). DARN/SuperDARN: A global view of the dynamics of high-latitude convection. *Space Science Reviews*, 71(1-4), 761–796. Doi:10.1007/BF00751350

Huang, C.-S., J. C. Foster, L. P. Goncharenko, P. J. Erickson, and W. Rideout (2005), A strong positive phase of ionospheric storms observed by the Millstone Hill incoherent scatter radar and global GPS network, *J. Geophys. Res.,* **110**, A06303, doi:10.1029/2004JA010865.

Jin, Y., Spicher, A., Xiong, C., Clausen, L. B. N., Kervalishvili, G., Stolle, C., Miloch, W. J. (2019) Ionospheric Plasma Irregularities Characterized by the Swarm Satellites: Statistics at High Latitudes. *J. Geophys. Res.,*124, 2, 1262−1282, doi: 10.1029/2018JA026063.

Jin, Y., C. Xiong, L. Clausen, A. Spicher et al (2020) Ionospheric plasma irregularities based on in-situ measurements from the Swarm satellites, *J. Geophys. Res.,*125, 7, e2020JA028103, doi: 10.1029/2020JA028103

Karpachev, A.T. M.V. Klimenko, V.V. Klimenko, L.V. Pustovalova. (2016) Empirical model of the main ionospheric trough for the nighttime winter conditions, *J. Atmospheric and Solar-Terrestrial Physics,* doi: 10.1016/j.jastp.2016.05.008.

Kelley, M. C., Vlasov, M. N., Foster, J. C., & Coster, A. J. (2004). A quantitative explanation for the phenomenon known as storm-enhanced density. *Geophysical Research Letters*, **31**, L19809. https://doi.org/10.1029/2004GL020875

Kelley, M. C., J. J. Makela, O. de La Beaujardière, and J. Retterer (2011), Convective ionospheric storms: A review, *Rev. Geophys.,* 49, RG2003, doi:10.1029/2010RG000340.

Kikuchi, T., & Hashimoto, K. K. (2016). Transmission of the electric fields to the low latitude ionosphere in the magnetosphere-ionosphere current circuit. Geoscience Letters, 3(1), 1–11. Doi:10.1186/s40562-016-0035-6.

Kikuchi, T., K. K. Hashimoto, and K. Nozaki (2008), Penetration of magnetospheric electric fields to the equator during a geomagnetic storm, *J. Geophys. Res.,* 113, A06214, doi:10.1029/2007JA012628

Lei, J., Wang, W., Burns, A. G., Yue, X., Dou, X., Luan, X., **...**Liu, Y. C.-M. (2014). New aspects of the ionospheric response to the October 2003 superstorms from multiple-satellite observations. Journal of Geophysical Research: Space Physics, 119(3), 2298–2317. https://doi.org/10.1002/2013JA019575

Lühr H., Warnecke JF, Rother MKA. (1996). An algorithm for estimating field-aligned currents from single spacecraft magnetic field measurements: a diagnostic tool applied to Freja satellite data. *IEEE Trans Geosci Remote Sens,* 34(6): 1369–1376. Doi:10.1109/36.544560.

Lühr, H., Park, J., Gjerloev, J. W., Rauberg, J., Michaelis, I., Merayo, J. M. G., & Brauer, P. (2015). Field- aligned currents' scale analysis performed with the Swarm constellation. *Geophysical Research Letters*, 42(1), 1–8. https://doi.org/10.1002/2014GL062453

Moffett, R. J., and S. Quegan (1983), The mid-latitude trough in the electron concentration of the ionospheric F-layer: A review of observations and modeling, *J. Atmos. Terr. Phys.*, 45, 315.

Ngwira, C. M., J.-B. Habarulema, E. Astafyeva, E. Yizengaw, O.F. Jonah, G. Crowley, A. Gisler, and V. Coffey. (2019) Dynamic response of ionospheric plasma density to the geomagnetic storm of 22-23 June 2015. *J. Geophys. Res. - Space Physics*, V. 124, 7123 - 7139, doi: 10.1029/2018JA026122.

Nishimura, Y., Mrak, S., Semeter, J. L., Coster, A. J., Jayachandran, P. T., Groves, K. M., et al. (2021). Evolution of mid-latitude density irregularities and scintillation in North America during the 7–8 September 2017 storm. *Journal of Geophysical Research: Space Physics*, 126, e2021JA029192, doi:10.1029/2021JA029192

Nishitani, N. et al., (2019), Review of the accomplishments of mid-latitude Super Dual Auroral Radar Network (SuperDARN) HF radars, *Progress in Earth and Planetary Science*, 6:27 https://doi.org/10.1186/s40645-019-0270-5.

Paxton, L.J., R. K. Schaefer, Y. Zhang, H. Kil, and J. E. Hicks (2018) SSUSI and SSUSI-Lite: Providing Space Situational Awareness and Support for Over 25 Years, *Johns Hopkins APL Technical Digest*, Volume 34, Number 3, 388-400, https://www.jhuapl.edu/Content/techdigest/pdf/V34-N03/34-03-Paxton.pdf

Pi, X., Mannucci A.J., Lindqwister U.J., Ho C.M. (1997) Monitoring of global ionospheric irregularities using the worldwide GPS network. *Geophys Res Lett.,* 24(18):2283–2286. doi:10.1029/97GL02273

Piersanti, M. et al. (2020) From the Sun to the Earth: August 25, 2018 geomagnetic storm effects, *Ann. Geophys.,* doi: 10.5194/angeo-2019-165

Ritter, P., Lühr, H., and Rauberg, J. (2013): Determining field-aligned currents with the Swarm constellation mission, Earth Planets Space, 65(11), 1285-1294, doi:10.5047/eps.2013.09.006.

Shen, X., Q. Zong, and X. Zhang, (2018), Introduction to special section on the China Seismo-Electromagnetic Satellite and initial results. *Earth Planetary Phys.*, 2, 439, https://doi.org/10.26464/epp2018041.

Spogli, L., Sabbagh, D., Regi, M., Cesaroni, C., Perrone, L., Alfonsi, L., et al. (2021). Ionospheric response over Brazil to the August 2018 geomagnetic storm as probed by CSES-01 and Swarm satellites and by local ground-based observations. Journal of Geophysical Research: Space Physics, 126, e2020JA028368. Doi: 10.1029/2020JA028368

Swarm Data Handbook, https://earth.esa.int/web/guest/missions/esa-eo-missions/swarm/data-handbook

Takahashi, H., et al (2015). Plasma bubble monitoring by TEC map and 630 nm airglow image. *J. Atmos. Sol.-Terr. Phys.*, N. 130-131, 151-158.

872 Thomas, E. G., J. B. H. Baker, J. M. Ruohoniemi, L. B. N. Clausen, A. J. Coster, J. C.
873   Foster, and P. J. Erickson (2013), Direct observations of the role of convection
874   electric field in the formation of a polar tongue of ionization from storm enhanced
875   density, *J. Geophys. Res. Space Physics*, **118**, 1180–1189,
876   doi:10.1002/jgra.50116

877 Tsurutani, B., et al. (2004), Global dayside ionospheric uplift and enhancement
878   associated with interplanetary electric fields, *J. Geophys. Res.*, 109, A08302,
879   doi:10.1029/2003JA010342.

880 Tsurutani, B. T., et al. (2006), The dayside ionospheric "superfountain" (DIS), plasma
881   transport and other consequences, *Proceedings of the ILWS Workshop 2006*, pp.
882   384–388, Goa, India, 19-24 Feb.

883 Valladares, C.E., J. Villalobos, R. Sheehan, and M. P. Hagan. (2004) Latitudinal
884   extension of low-latitude scintillations measured with a network of GPS receivers,
885   *Annales Geophysicae*, 22: 3155–3175

886 Valladares, C. E., Eccles, J. V., Basu, S., Schunk, R. W., Sheehan, R., Pradipta, R.,
887   & Ruohoniemi, J. M. (2017). The magnetic storms of 3–4 August 2010 and 5–6
888   August 2011: 1. Ground- and space-based observations. *J. Geophys. Res. Space
889   Physics*, 122, 3487– 3499. https://doi.org/10.1002/2016JA023359

890 Vanlommel, P. (2018) Solar-Terrestrial Centre of Excellence (STCE) Newsletter, 20-26
891   Aug 2018, http://www.stce.be/newsletter/pdf/2018/STCEnews20180831.pdf

892 Wang, S., W. Cheng, D. Yang, D. Liu (2019) Preliminary validation of in situ electron
893   density measurements onboard CSES satellite using observations from Swarm
894   Satellites. *Advances in Space Research*, V. 64, N4, pp.982-994. Doi:
895   10.1016/j.asr.2019.05.025.

896 WDC-Kyoto (2018a) http://wdc.kugi.kyoto-u.ac.jp/ae_realtime/201808/index_201808
897   25.html

898 WDC-Kyoto (2018b) http://wdc.kugi.kyoto-u.ac.jp/ae_realtime/201808/index_201808
899   26.html

900 Wessel, P., J.F. Luis, L. Uieda, R. Scharroo, F. Wobbe, W.H.F. Smith, D. Tian (2019)
901   The Generic Mapping Tools Version 6. *Geochemistry, Geophysics, Geosystems*.
902   V. 20, N11, Doi: 10.1029/2019GC008515

903 Xiong, C, H. Lühr, H. Wang, and M.G. Johnsen. (2014) Determining the boundaries of
904   the auroral oval from CHAMP field-aligned current signatures-Part I, *Ann.
905   Geophys.*, 32, 609-622. Doi:10.5194/angeo-32-609-2014.

906 Xiong, C, F. Lin, X. Luo, Yaqi Jin, and Xin Wan (2019). Plasma patches inside the polar
907   cap and auroral oval: the impact on the spaceborne GPS receiver. *J. Space
908   Weather Space Clim., 9, A25*, doi: 10.1051/swsc/2019028

909 Yasyukevich, Yu., E. Astafyeva, A. Padokhin, V. Ivanova, S. Syrovatskii, A. Podlesnyi.
910   (2018) The 6 September 2017 X-class solar flares and their impacts on the
911   ionosphere, GNSS and HF radio wave propagation. *Space Weather*, V.16, 1013-
912   1027, doi: 10.1029/2018SW001932

913   Yasyukevich Yu.V., Vesnin A.M., Perevalova N.P. (2018) SibNet – Siberian Global
914   Navigation Satellite System Network: Current state. Solar-Terrestrial Physics. V. 4,
915   N 4. P. 63–72. DOI: 10.12737/stp-44201809

916   Yasyukevich, Y.V., Kiselev, A.V., Zhivetiev, I.V. et al. (2020a) SIMuRG: System for
917   Ionosphere Monitoring and Research from GNSS. *GPS Solutions,* 24, 69.

918   Yasyukevich, Yu., R. Vasilyev, K. Ratovsky, A. Setov, M. Globa et al. (2020b) Small-
919   Scale Ionospheric Irregularities of Auroral Origin at Mid-latitudes during the 22
920   June 2015 Magnetic Storm and Their Effect on GPS Positioning, *Remote*
921   *Sensing*, 12, doi: 10.3390/rs12101579.

922   Yizengaw, E., H. Wei, M. B. Moldwin, D. Galvan, L. Mandrake, A. Mannucci, and X. Pi
923   (2005), The correlation between mid-latitude trough and the plasmapause,
924   *Geophys. Res. Lett.*, 32, L10102, doi:10.1029/2005GL022954.

925   Yizengaw, E., M. B. Moldwin, and D. A. Galvan (2006), Ionospheric signatures of a
926   plasmaspheric plume over Europe, *Geophys. Res. Lett*., 33, L17103,
927   doi:10.1029/2006GL026597.

928   Zakharenkova, I. and E. Astafyeva. (2015) Topside ionospheric irregularities as seen
929   from multi-satellite observations. *J. Geophys. Res. - Space Physics*, V.120, N1,
930   807-824, doi:10.1002/2014JA020330.

931   Zakharenkova, I., E. Astafyeva and Iu. Cherniak. (2016a) GPS and in situ Swarm
932   observations of the topside equatorial plasma irregularities. *Earth Planets and*
933   *Space*, V.68, doi:10.1186/s40623-016-0490-5.

934   Zakharenkova, I., E. Astafyeva and Iu. Cherniak. (2016b) GPS and GLONASS
935   observations of traveling ionospheric disturbances during the 2015 St. Patrick's
936   Day storm, *J. Geophys. Res.*, V.121, N12, 12,138-12,156,
937   doi:10.1002/2016JA023332.

938   Zakharenkova, I. E. et al. (2019) Features of Storm-Induced Ionospheric Irregularities
939   From Ground-Based and Spaceborne GPS Observations During the 2015 St.
940   Patrick's Day Storm, *J. Geophys. Res.- Space Physics, doi:*
941   10.1029/2019JA026782

942   Zakharenkova, I., & Cherniak, I. (2020). When plasma streams tie up equatorial plasma
943   irregularities with auroral ones. *Space Weather*, 18, e2019SW002375.
944   https://doi.org/10.1029/2019SW002375

945   Zhou, F., et al., (2018) GAMP: An open-source software of multi-GNSS precise point
946   positioning using undifferenced and uncombined observations, *GPS Solutions*,
947   **22**(33), doi:10.1007/s10291-018-0699-9.

948   Zou et al., (2014) On the generation/decay of the storm-enhanced density plumes:
949   Role of the convection flow and field-aligned ion flow, *J. Geophys. Res*., V. 119,
950   N110, p. 8543-8559, doi: 10.1002/2014JA020408

951   Zou, S., A. J. Ridley, M. B. Moldwin, M. J. Nicolls, A. J. Coster, E. G. Thomas, and J.
952   M. Ruohoniemi (2013), Multi-instrument observations of SED during 24–25
953   October 2011 storm: Implications for SED formation processes, *J. Geophys. Res.*
954   *Space Physics*, **118**, 7798– 7809, doi:10.1002/2013JA018860.

Figure Captions
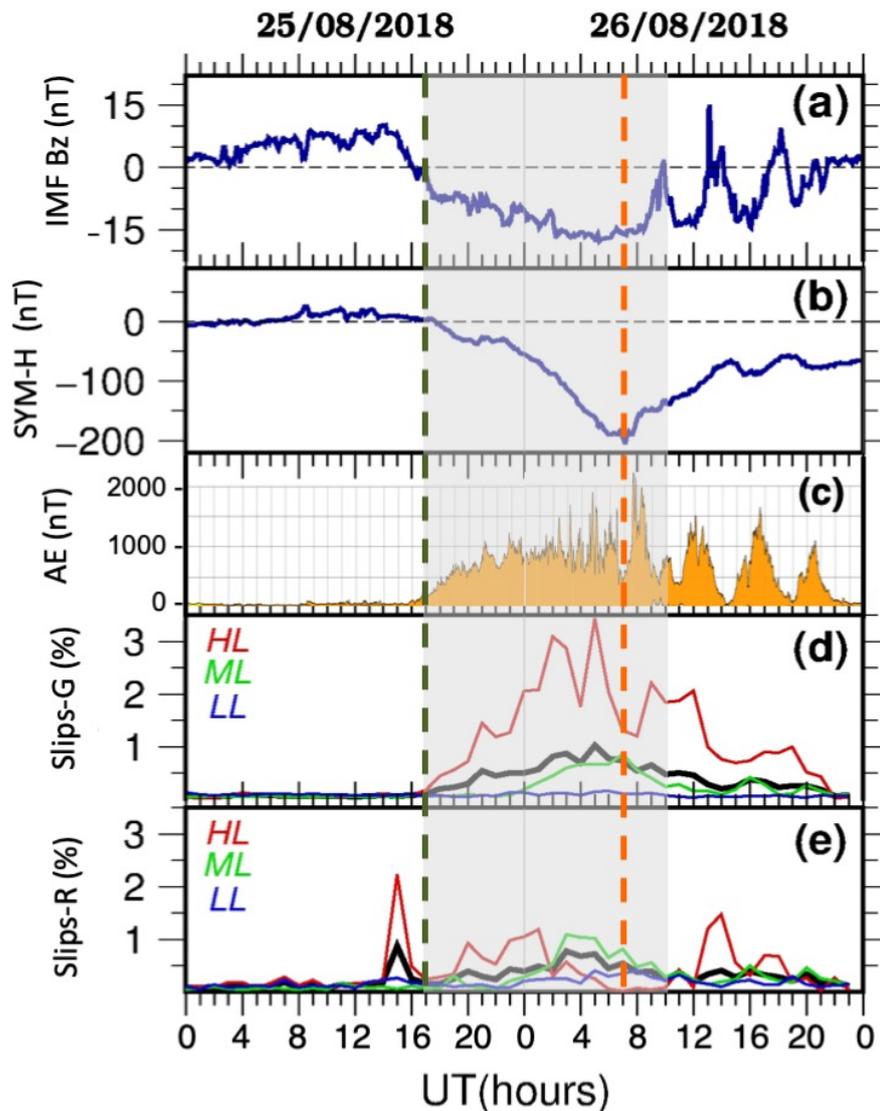
956

957   **Figure 1. (a-c)** Variations of interplanetary and geophysical parameters during the
958   geomagnetic storm of 25-26 August 2018: **(a)** the north-south (Bz) component of the
959   interplanetary magnetic field (IMF) in GSM coordinates; **(b)** – SYM-H index; **(c)** the
960   auroral electrojey (AE) index [WDC-Kyoto, 2018a; 2018b]; **(d, e)** the percentage of
961   TEC slips for GPS and Glonass satellites, respectively. The solid black curves show
962   the global value, red – the TEC-slips at high latitudes (HL), green – at middle latitudes
963   (ML) and blue – at low-latitudes (LL). The IMF-Bz and SYM-H data are 5-min cadence,
964   and the TEC Slips data are 1-hr cadence. Orange and dark green dotted vertical lines
965   denote the beginning of the main and recovery phases of the storm. Gray shaded
966   rectangle depicts the period of time analysed in detail in this work.
967
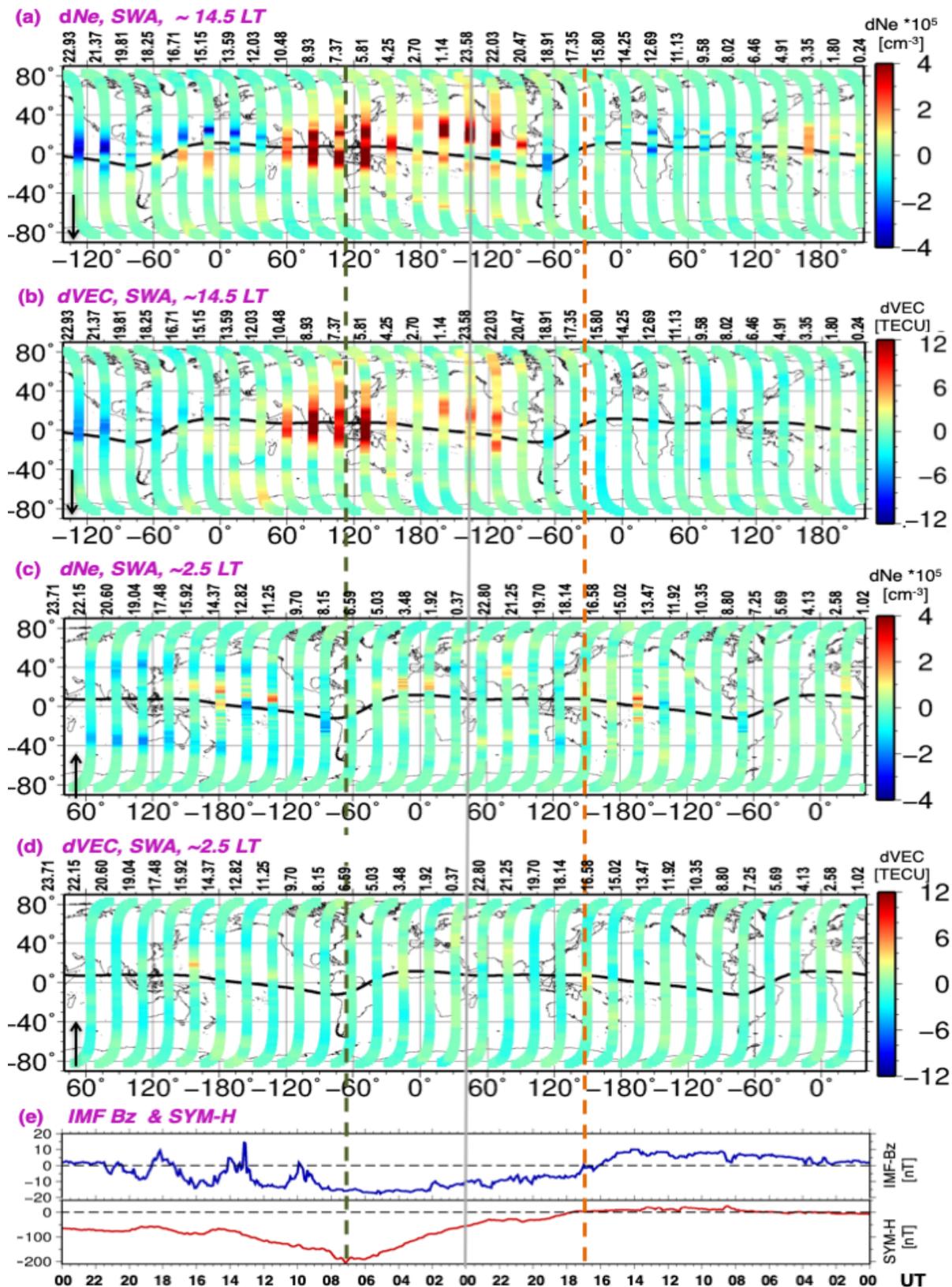
Figure 2. (a-d) Storm-time variations of the vertical electron content (dVEC) and Electron density (dNe) as measured by SWA in the daytime (~14.4LT, **a-b**) and night-time (~2.4LT, **c-d**) sectors. The orbital altitude is 430-460 km. The times of the equatorial crossings in UT is shown on the top of each panel. Black curve denotes

973 the position of the magnetic equator **(e)** Variations of the IMF Bz & SYM-H. Note that
974 the UT scale is directed from right to the left. Orange and dark green dotted vertical
975 lines denote the beginning of the main and recovery phases of the storm. We note
976 that all SWA observations, during the main and the recovery phases of the storm,
977 correspond in time and location to the effects observed by the GNSS-TEC.

978
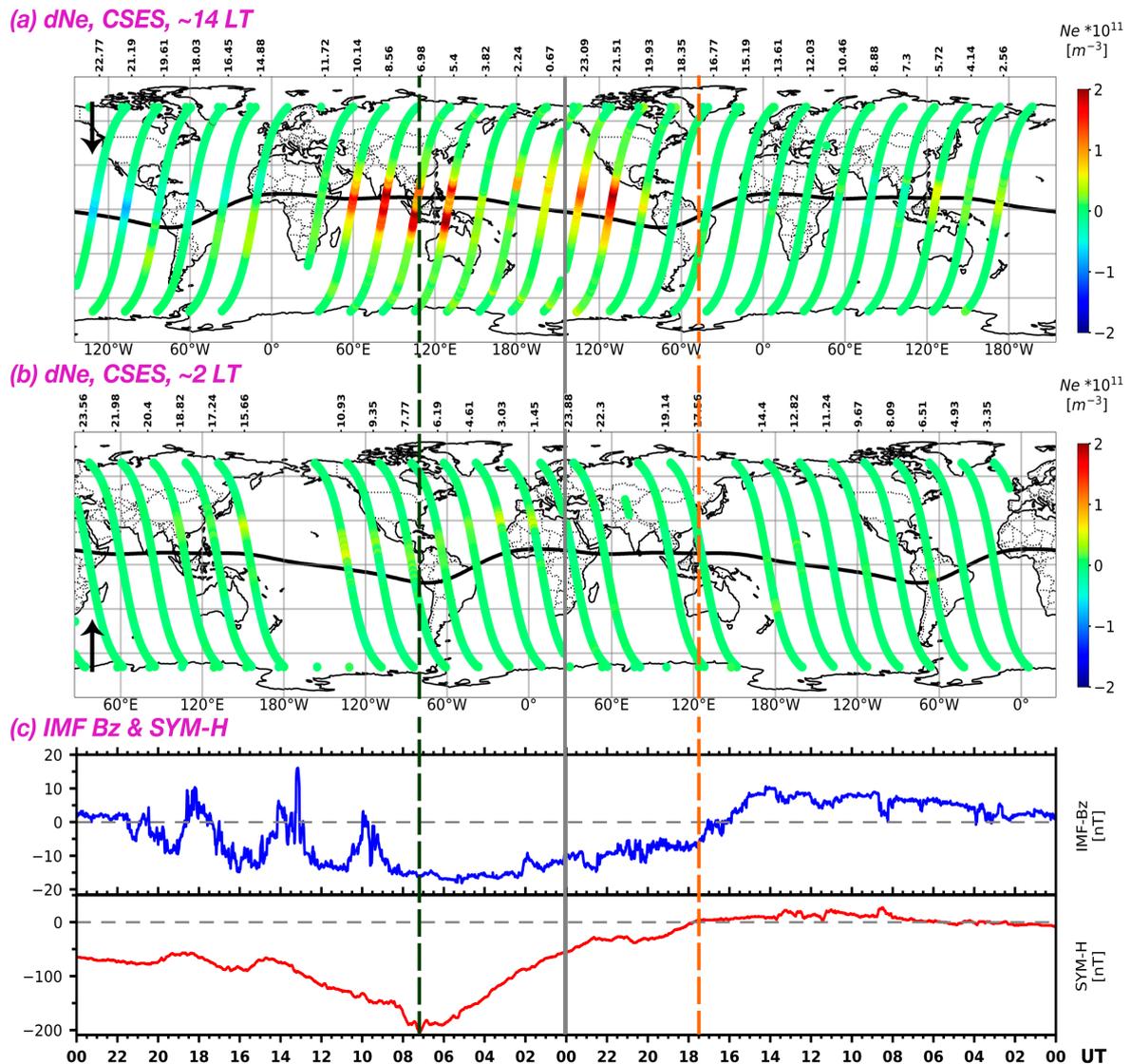
980 **Figure 3. (a-b)** Storm-time variations of the electron density (dNe) as measured by
981 the Langmuir Probe onboard CSES spacecraft in the daytime (14LT) and night-time
982 sector (2LT for CSES). The orbital altitude varied between 507 and 524 km. **(c)**
983 Variations of the IMF Bz & SYM-H. Note that the UT scale is directed from right to the
984 left. Orange and dark green dotted vertical lines denote the beginning of the main and
985 recovery phases of the storm.

986
987
988
989
990
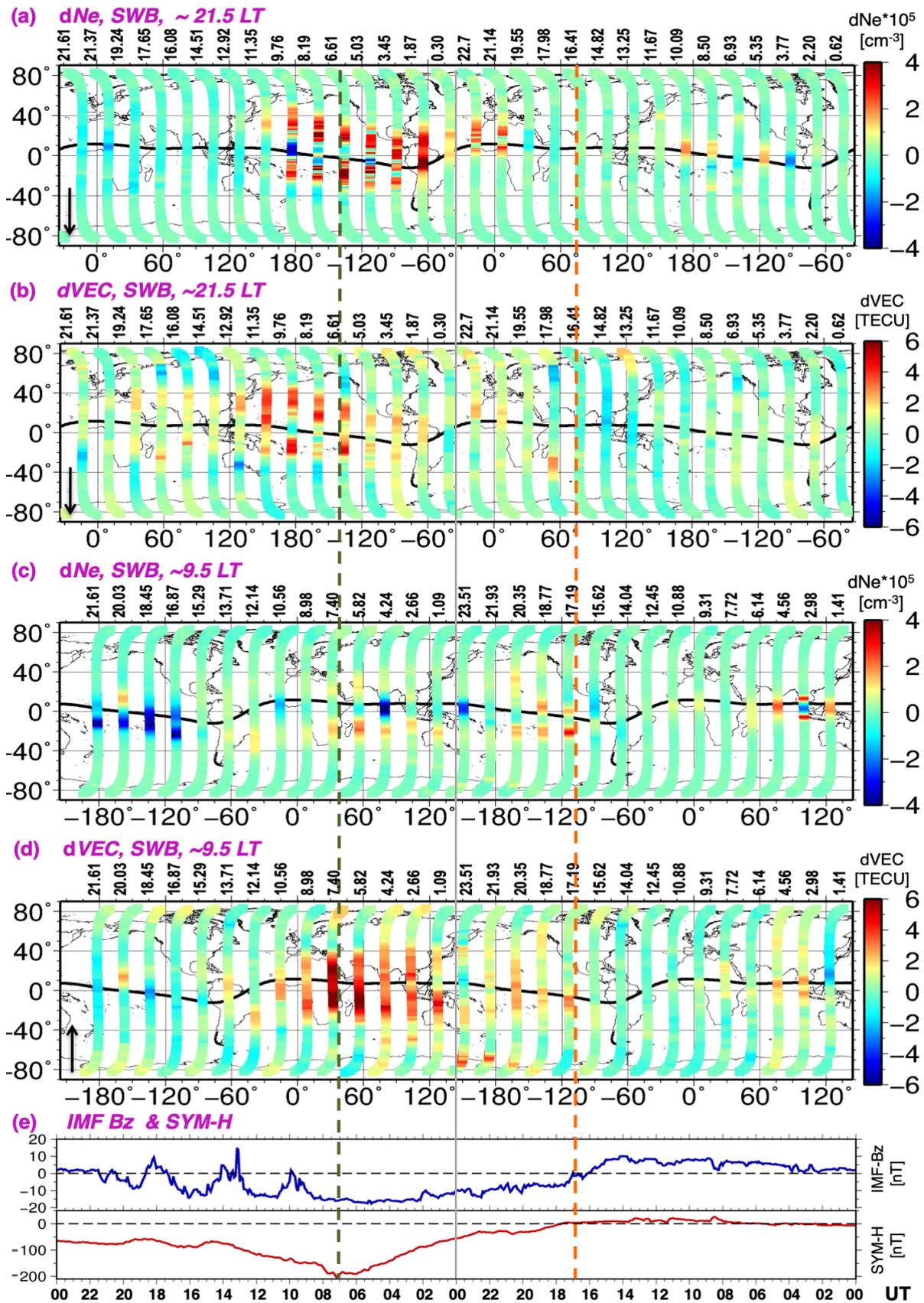
Figure 4. Same as Figure 2, but for Swarm B satellite. The SWB crosses the equator at ~21.6LT (**a-b**) and ~9.6LT (**c-d**). The orbital altitude varied between 498 and 525 km. **(e)** Variations of the IMF Bz &SYM-H. Note that the UT scale is directed from right to the left.

996
997 **Figure 5. (a-g)** The key features of the ionospheric storm on 25-26 August 2018 as
998 derived from the ground-based GPS-receivers. The storm-time values (dVTEC) are
999 calculated with respect to the 7-day averaged quiet-time reference value. The
1000 corresponding time and the date are shown on the top of each panel, the color scale
1001 is shown on the right. Panel **(h)** shows variations of the IMF-Bz (blue curve) and the
1002 SYM-H index (red curve) versus the UT for the days of the storm 25-26 August. Green
1003 arrows indicate the moments of time mentioned in panels (a-g).
1004
1005
1006
1007
1008
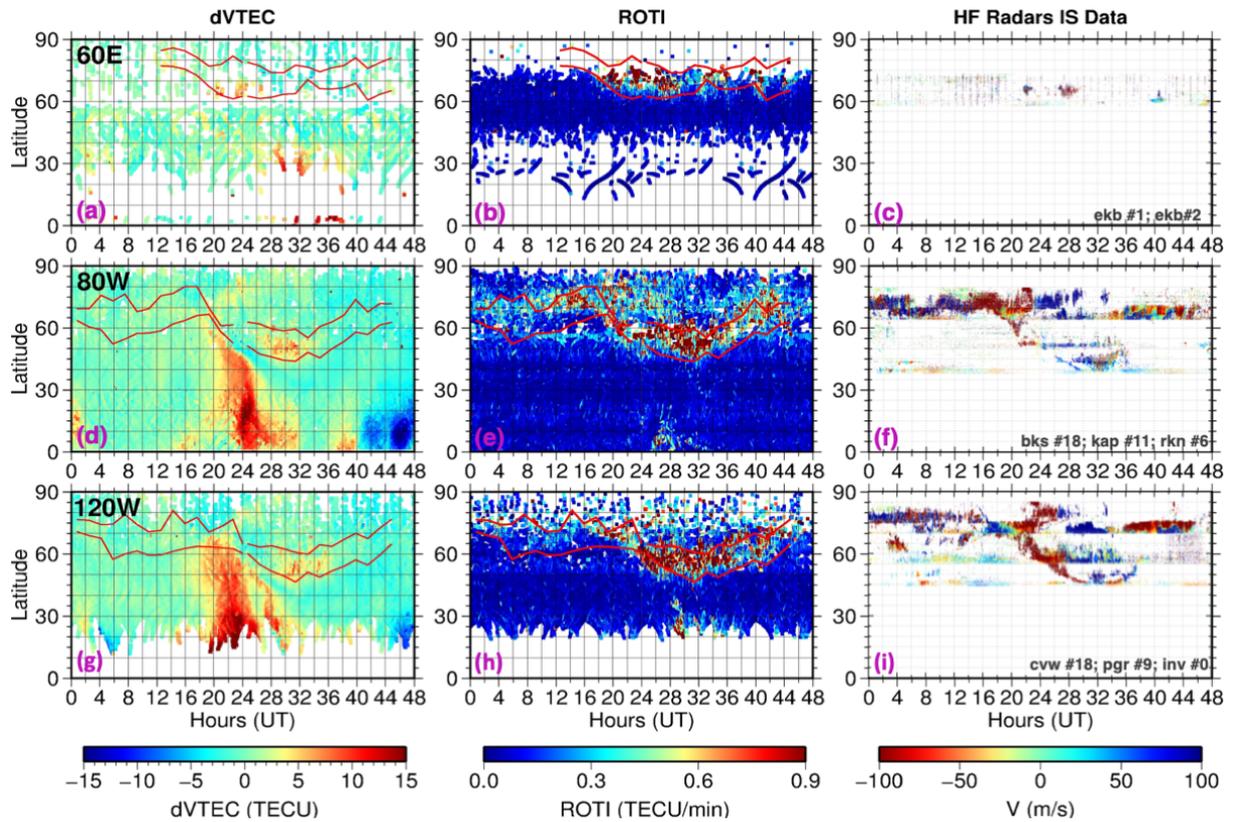
Figure 6. Variations of dVTEC, ROTI, and Doppler velocity data along the longitudes: 60°E (a, b, c), 80°W (d, e, f) and 120°W (g, h, i). The corresponding color scales are shown on the bottom. The Doppler velocities data are registered by the radars: (c) *ekb* (beams #1 and #2), (f) *bks* (beam #18*)*, *kap* (#11), *rkn* (#6) and (i) *cvw* (#18), *pgr* (#9), *inv* (#0). Red thick curves show the positions of the auroral oval polarward and equatorward boundaries.
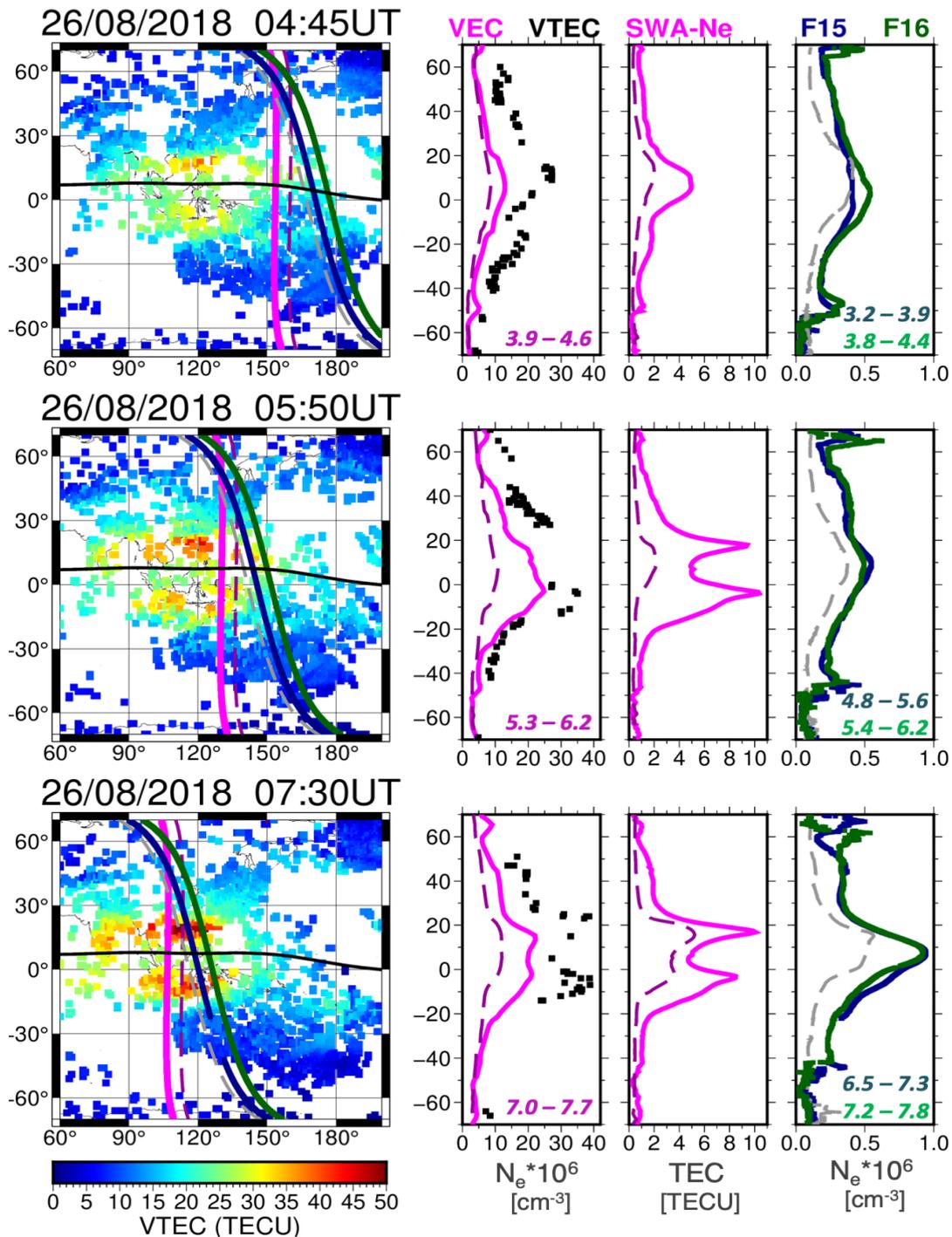
Figure 7. Positive ionospheric storm over Asian-Australian region at 4-8 UT on 26 August: the left panels show maps of the GNSS-derived absolute VTEC. Black thick line depicts the position of the magnetic dip equator. Colored traces show the trajectories of the satellites flying over this region during these moments of time (magenta- Swarm A, dark blue – DMSP F15, dark green – DMSP F16) and on the day before (dotted lines). Panels on the right show values of the topside TEC (VEC) measured by SWA in comparison with the VTEC along the SWA trajectory (black dots), and the in-situ Ne measurements effectuated by SWA at ~430 km of altitude (middle panels) and DMSP at ~840km (the right column of panels). Dotted curves depict quiet-time VEC and Ne values. Numbers on the panels show the UT of the beginning and the end of the satellite passes.
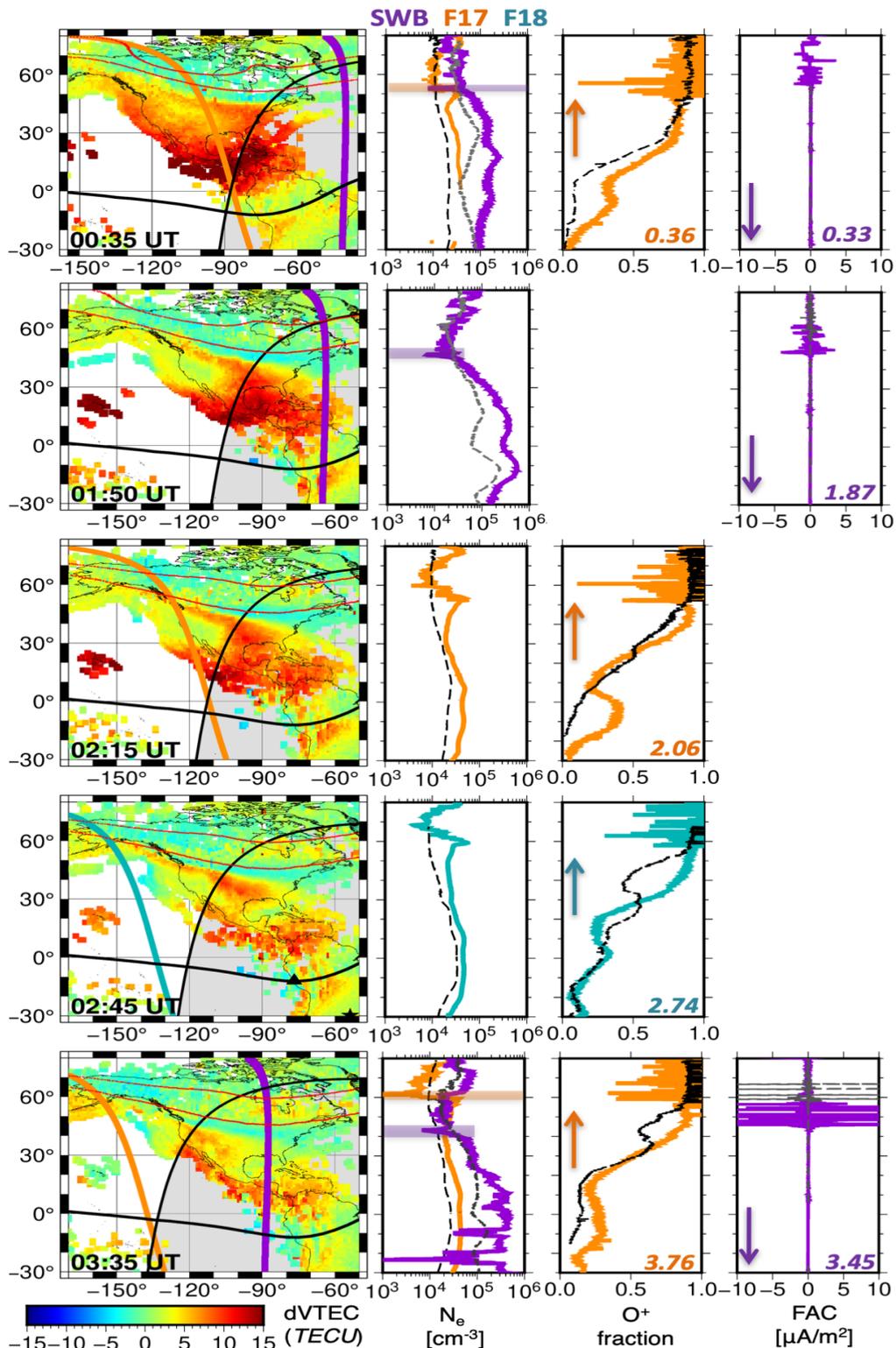
Figure 8. Ionospheric effects observed in the American region between 00:35 and 03:35UT. The left column of panels shows maps with dVTEC, the color scale is shown on the bottom. Coloured curves on the maps depict the trajectories of satellite orbit (SWB= violet, DMSP F17=orange, DMSP F18=teal). The corresponding UT is shown in the left bottom corner of each map. Black thick curve shows the geomagnetic equator. Thin red curves show the position of the polar and equatorial boundaries of the auroral oval as obtained from the GUVI model and DMSP data (https://ssusi.jhuapl.edu/gal_edr-aur_cs). The second column of panels shows

satellite observations: the in-situ electron density at the altitude of ~510 km (SWB, violet) and ~850 km (F17, orange and F18, teal). Dotted black and dark gray lines show quiet-time values. Shaded rectangles show the MIT. Column 3 depicts O+ fraction as measured by DMSP satellites. The rightmost column of panels shows FACs as estimated from measurements by SWB satellite. The UT time of the equatorial crossings are shown in the right bottom corner of each panel.
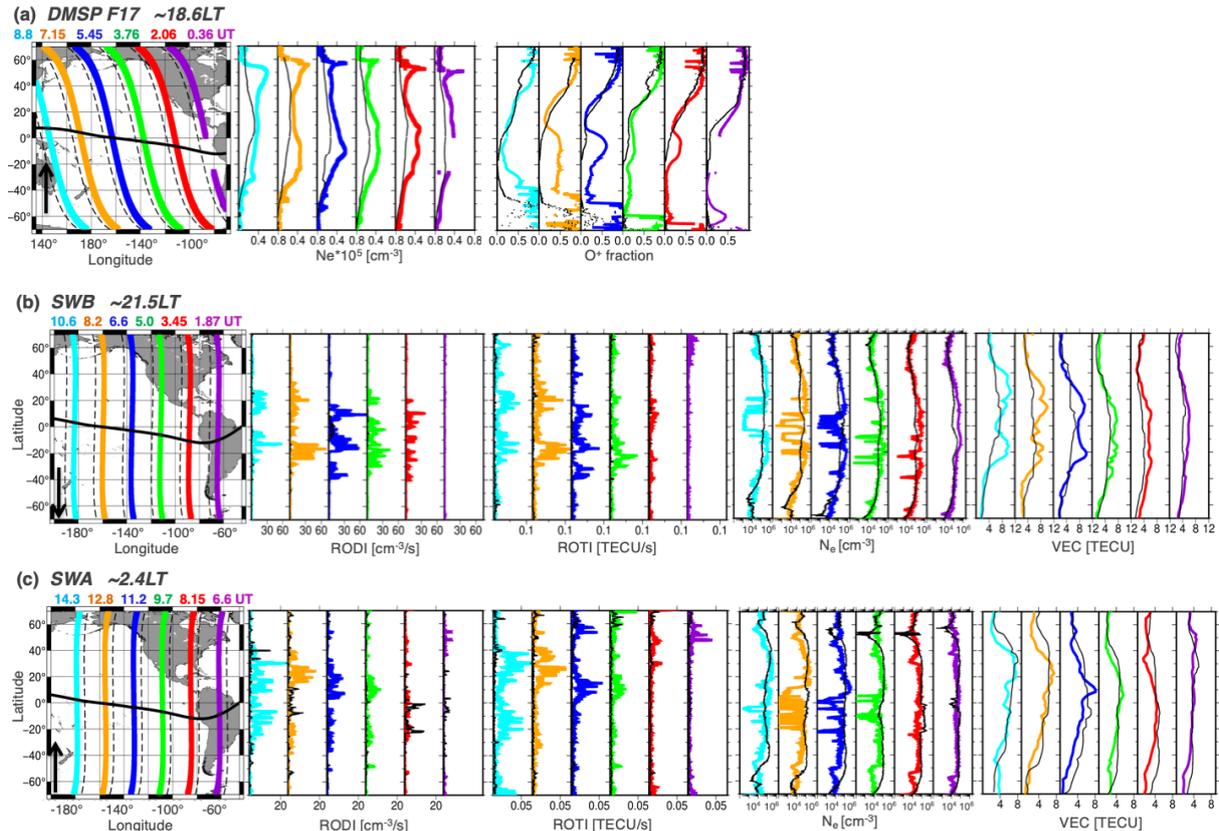

Figure 9. Ionospheric disturbances and irregularities observed over the Pacific region at the end of the main phase and beginning of the recovery phase of the storm: **(a)** DMSP F17 satellite, **(b)** SWB in 21.5LT sector, **(c)** SWA in 2.4LT sector.
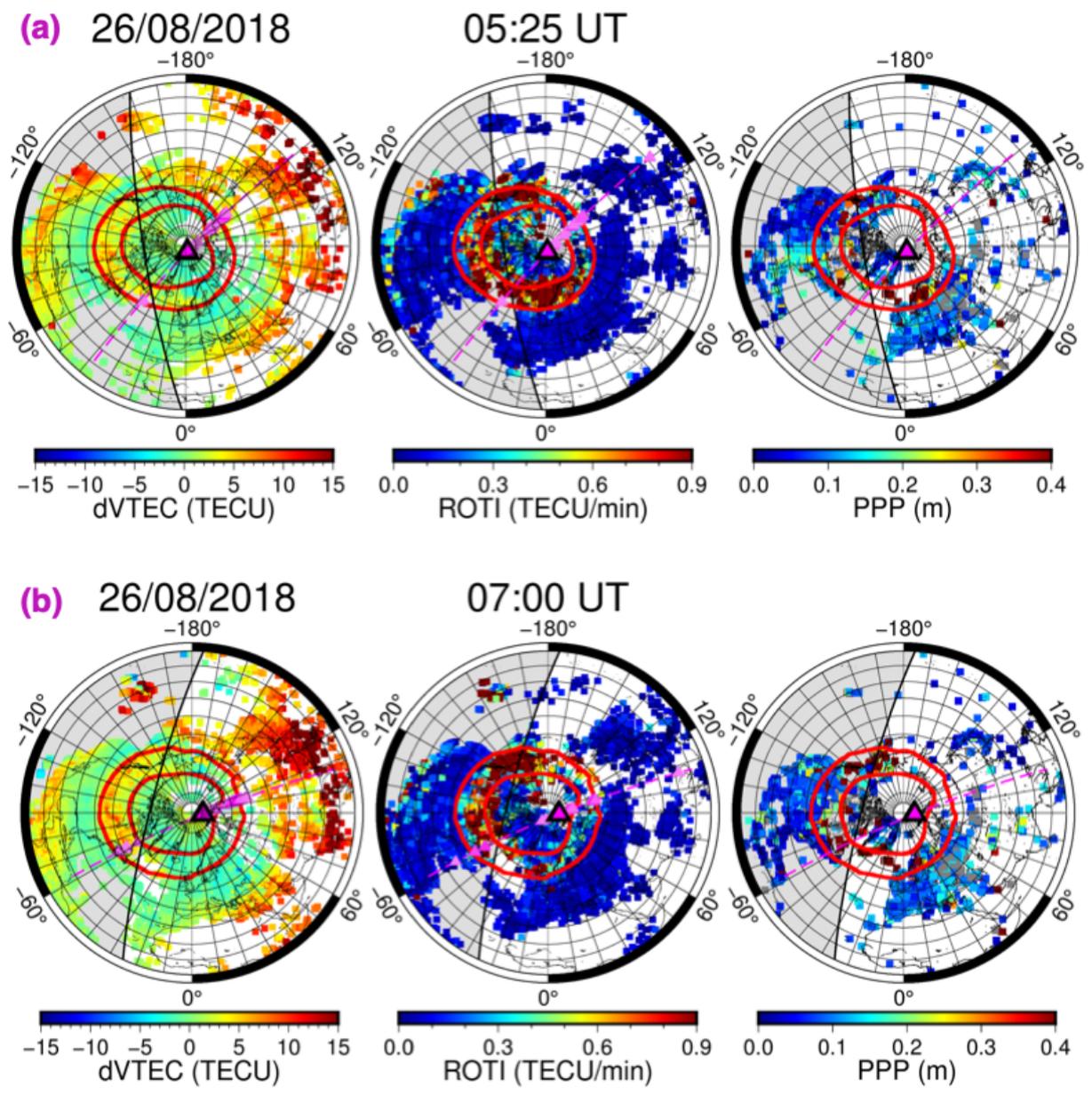
Figure 10: Maps of dVTEC (left), ROTI (middle) and precise point positioning (PPP, right) estimated at GPS-stations for the moments of time **(a)** 05:25UT and **(b)** 07:00UT in the NH. Thin red lines show the equatorward and poleward boundaries of the auroral oval. Magenta triangles show locations of intensified SROTI (left), RODI (middle) and FACs (right) as estimated from SWA data (±20 min from the moment of time indicated on the top of the panel for which the dVTEC, ROTI and PPP maps were plotted).
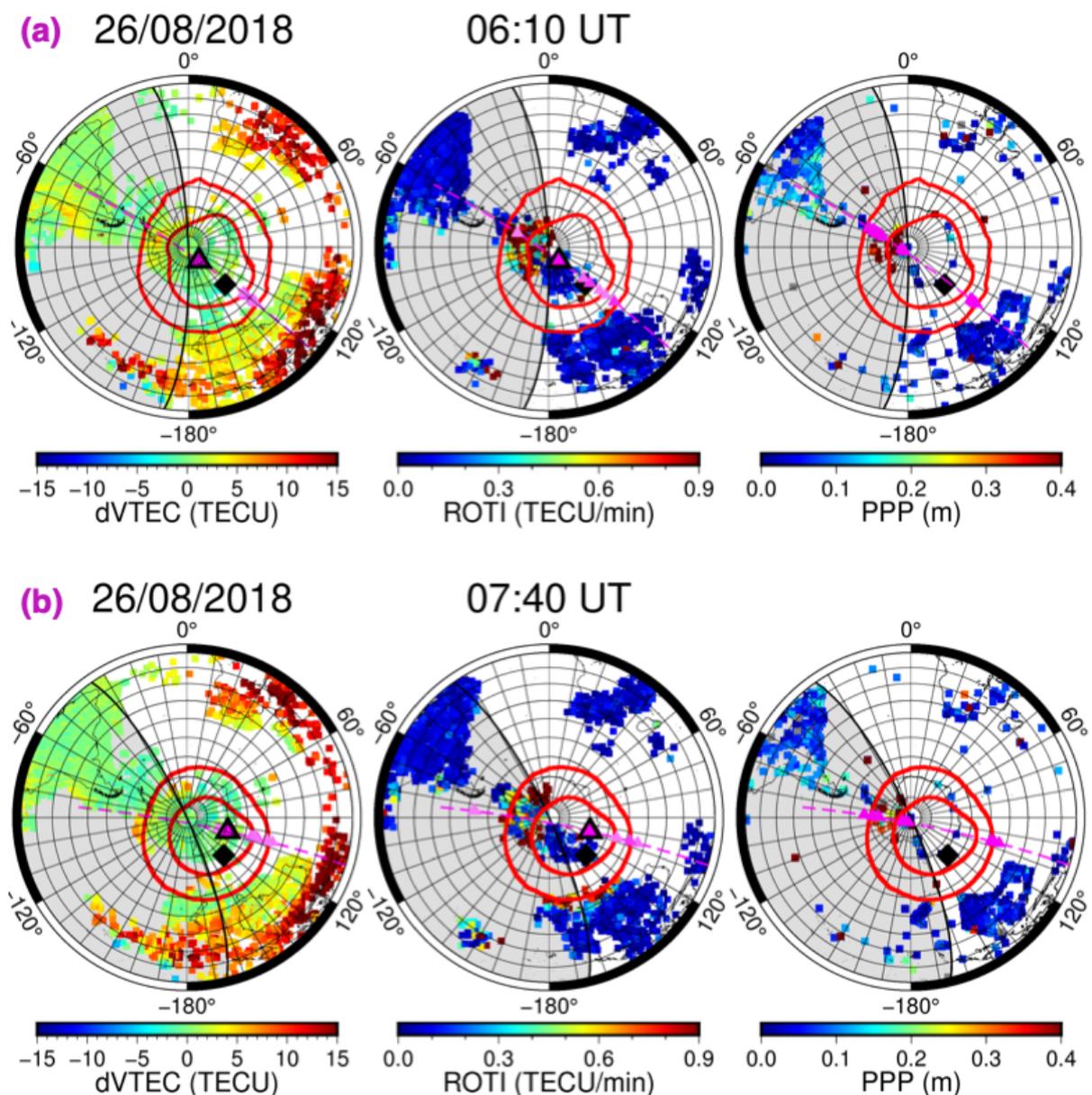
Figure 11. Same as Figure 9 but for the SH and moments of time **(a)** 06:10UT and **(b)** 07:40UT.

Supplementary Material contains 6 Figures and 2 animations.

Figure S1. (a-b) Measurements of the in-situ electron density Ne performed by the CSES satellite during the day (a) and night (b) passes; **(c-d)** The reference Ne map presenting the quiet-time values for day (c) and night (d). The reference map was calculated based on satellite passes during geomagnetically quiet days: 1-12, 21-24 and 29-31 August 2018. The data of the CSES mission are available through the Center for Satellite Application in earthquake Science of China (http://www.leos.ac.cn/).
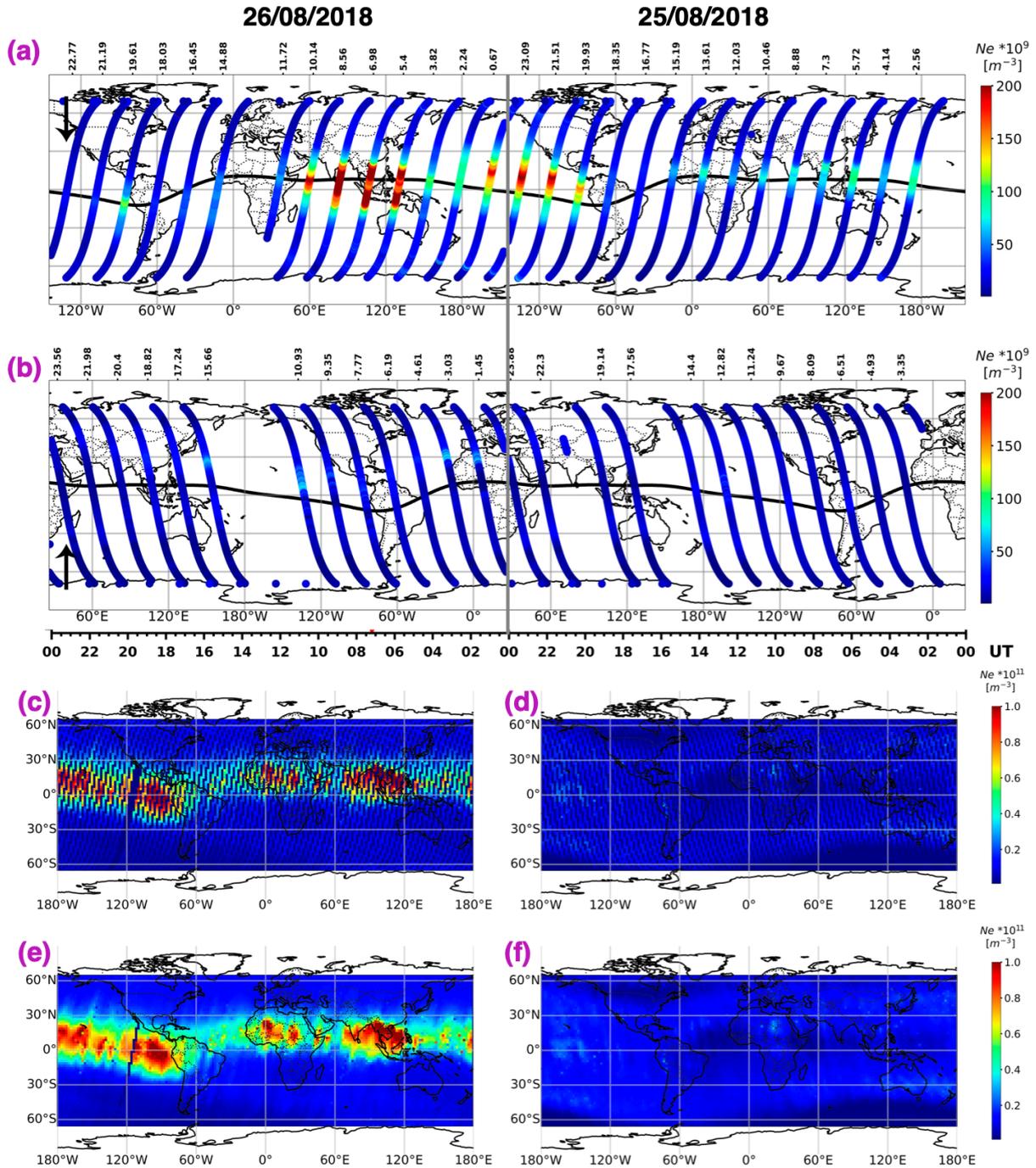
**Figure S2. (a-d)** Variations of vertical electron content (VEC) and in-situ Electron density (Ne) as measured by SWA in the daytime (~14.4LT, **a-b**) and night-time (~2.4LT, **c-d**) sectors. The orbital altitude is 430-460 km. The times of the equatorial crossings in UT is shown on the top of each panel. Black curve denotes the position of the magnetic equator. **(e)** Variations of the IMF Bz & SYM-H. Note that the UT scale is directed from right to the left. Orange and dark green dotted vertical lines denote the

1084   beginning of the main and recovery phases of the storm. We note that all SWA
1085   observations, during the main and the recovery phases of the storm, correspond in
1086   time and location to the effects observed by the GNSS-TEC. The data of the Swarm
1087   mission are available through the European Space Agency EarthNet data service

(http://earth.esa.int/swarm).

(a) *Ne, SWA, ~ 14.5 LT*

(b) *VEC, SWA, ~14.5 LT*

(c) *Ne, SWA, ~2.5 LT*

(d) *VEC, SWA, ~2.5 LT*

(e) *IMF Bz & SYM-H*

1089
1090
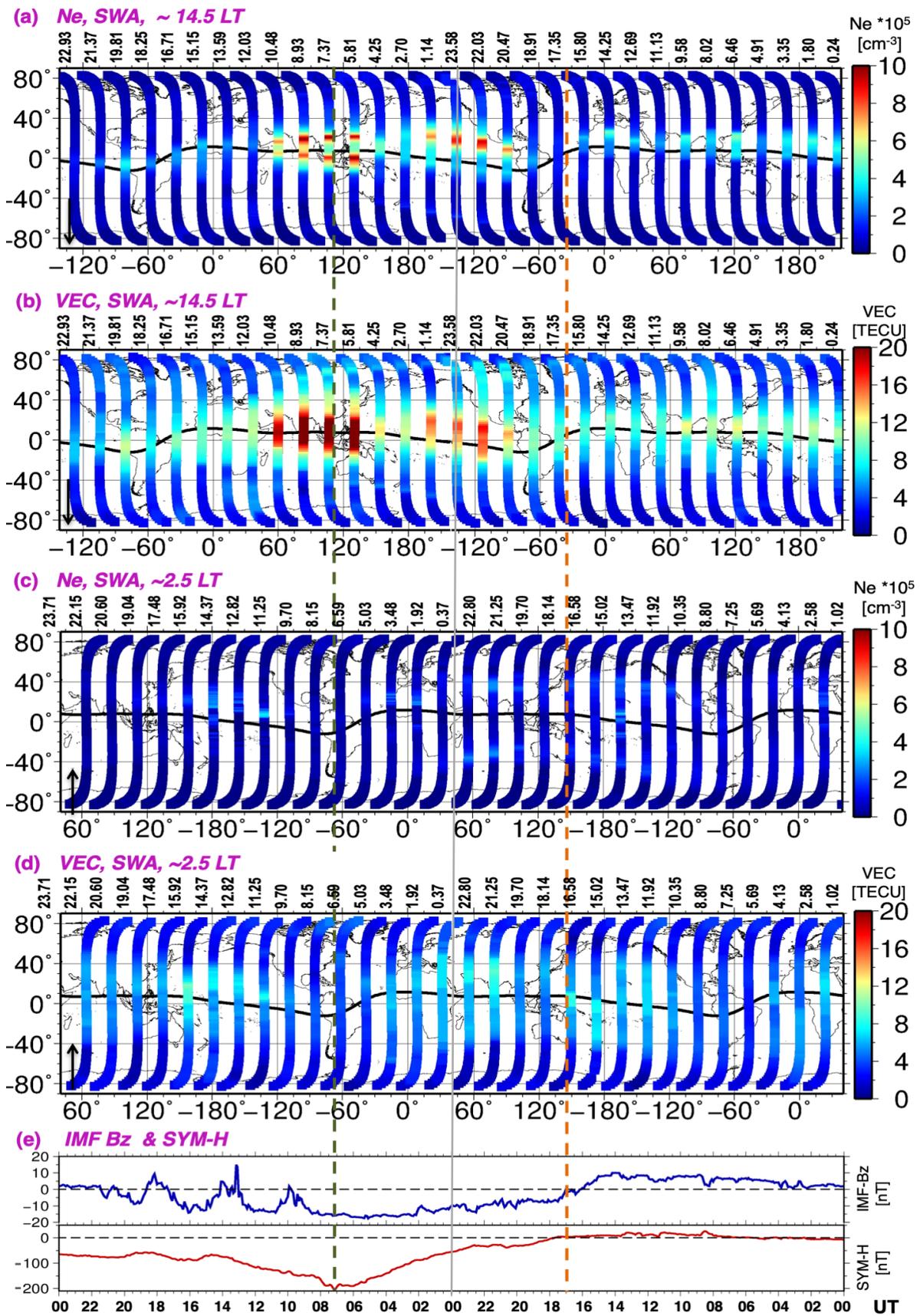
Figure S3. Same as Figure S2 but for SWB at ~21.6LT(**a-b**) and ~9.6LT (**c-d**). The
orbital altitude varied between 498 and 525 km.
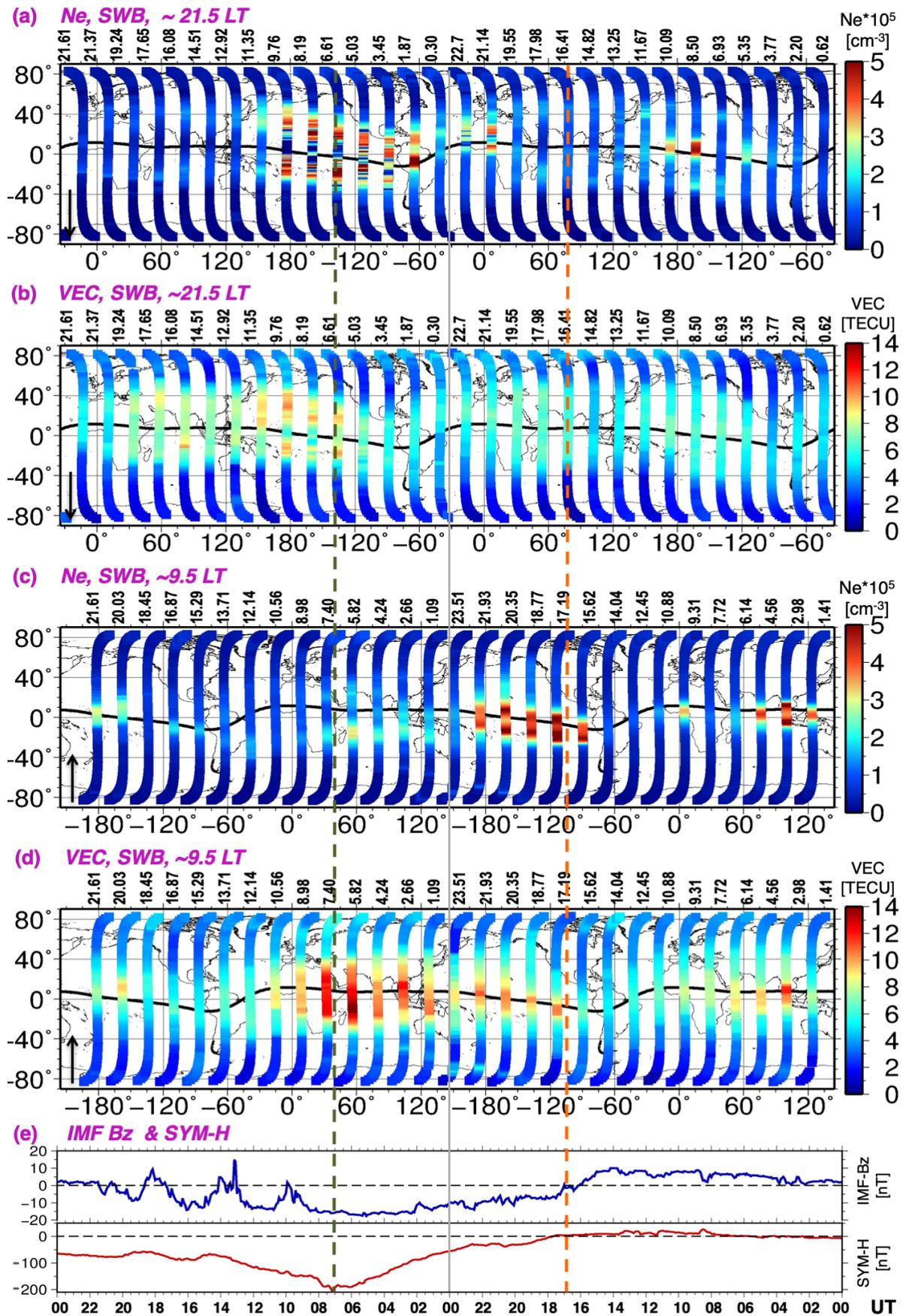
1094 **Figure S4.** Doppler velocities as retrieved from data of HF-radars (SuperDARN) at
1095 00:27UT **(a)**, 02:04UT **(b)**, 03:46UT **(c)** and 05:36 UT **(d)** on 26 August 2018. Red thin
1096 curved show the boundaries of the auroral oval. Black lines depict the position of the
1097 solar terminator.
1098
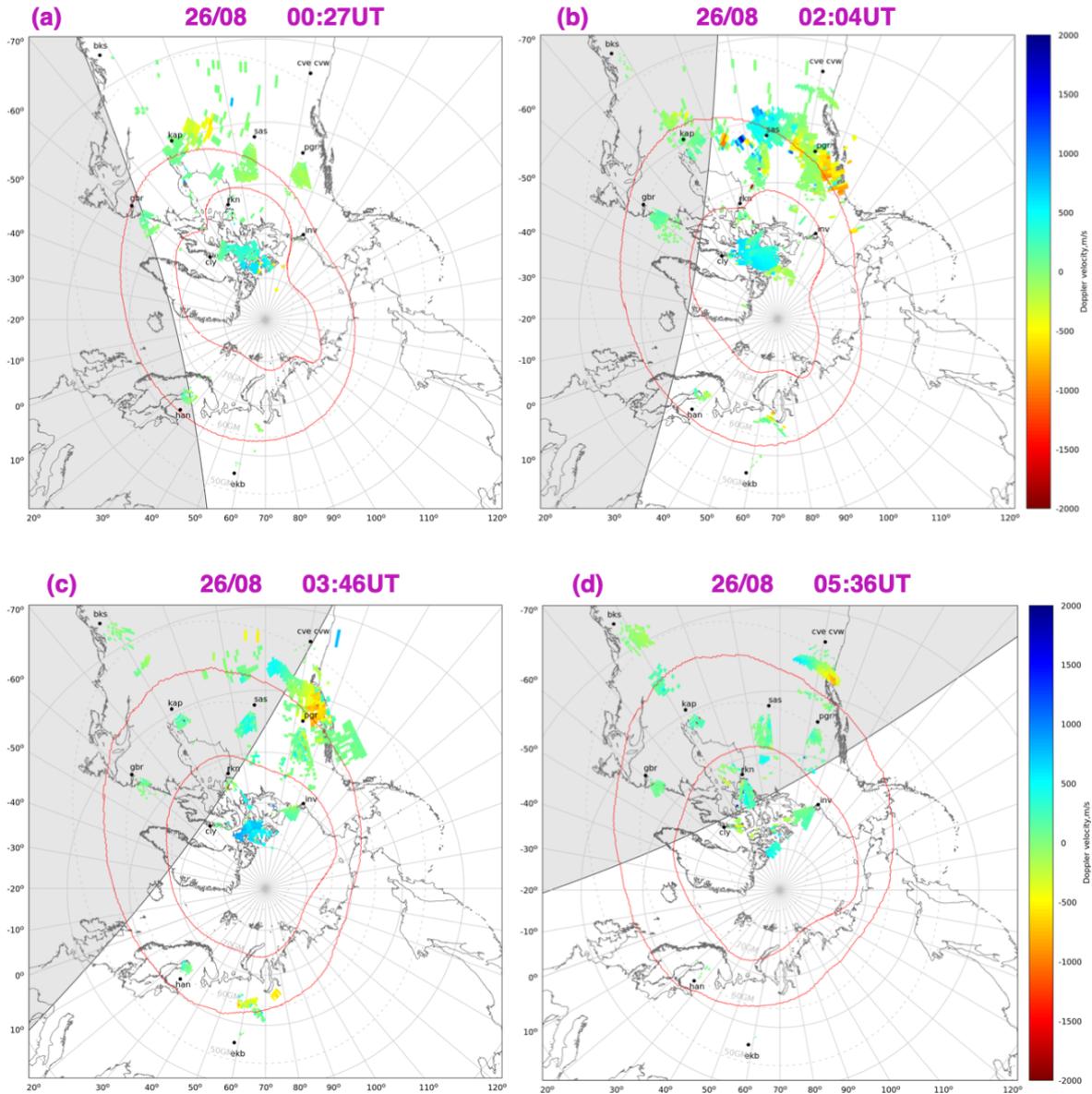
1099
1100
1101
1102
1103
1104
1105
1106
1107

Figure S5. Maps of VTEC (column **(a)**) and ROTI (column **(b)**) over American region between 01:50 and 03:35UT on 26 August 2018. In VTEC data, one can clearly see the occurrence of plasma bubbles mapping into the equatorial and low-latitude enhancement. The ROTI index increases at low and mid-latitudes in the northern hemisphere, however, we do not see signatures of plasma bubbles. Column (c) – Ionograms from the Digisonde Station at the Jicamarca Observatory (76.8W; 12S). The location of the ionosonde is shown by black triangle on the right panels.
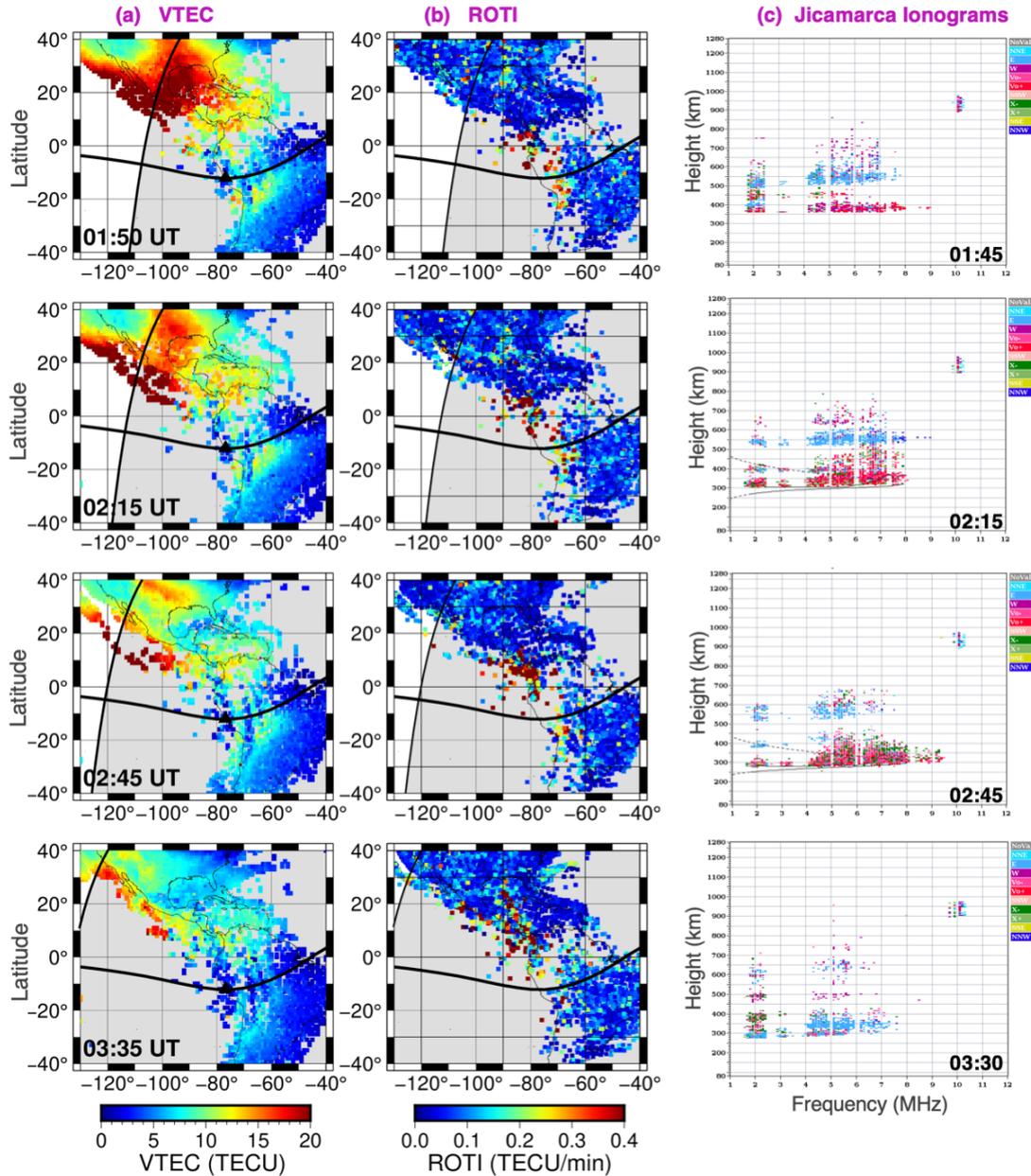
1121 **Figure S6. (a-g)** Precise Point Positioning (PPP) errors during the 25-26 August 2018
1122 storm. The corresponding time and the date are shown on the top of each panel, the
1123 color scale is shown on the right. The black curve denotes the position of the magnetic
1124 equator; Panel **(h)** shows variations of the IMF-Bz (blue curve) and the SYM-H index
1125 (red curve) versus the UT for the days of the storm 25-26 August. Green arrows
1126 indicate the moments of time mentioned in panels (a-g).

1127